Figure 5 Effect of GST-tagged human DJ-1 (GST-DJ-1) on oxidative and nitrosative stress induced by cerebral ischemia and reperfusion. (A to P) Representative photographs showing brain sections at +1 mm anterior from the bregma, which were immunostained with antibody against nitrotyrosine in sham-operated rats ($n = 4$) (A, E, I, and M) and ischemic rats at 7 days after MCAO, which had been injected with PBS ($n = 8$) (B, F, J, and N), GST (320 pmol; $n = 7$) (C, G, K, and O), or GST-DJ-1 (320 pmol; $n = 9$) (D, H, L, P) at 110 mins after the onset of MCAO. (Q to S) The number of nitrotyrosine-immunopositive cells in the boundary zones of the ischemic core in the cerebral cortex (CCb) (E to H and Q) and the striatum (STb) (I to L and R), and in the ischemic core in the striatum (STc) (M to P and S) was measured as an index of the level of oxidative and nitrosative stress. Data are the mean $\pm$ s.e.m. Significance (Bonferroni/Dunn *post hoc* comparisons after ANOVA): *$P < 0.05$ versus PBS-injected ischemic rats. †$P < 0.05$ versus GST-injected ischemic rats. Scale bars: 1 mm (A to D) and 200 μm (E to P).

GST immunoreactivity for exogenous GST-DJ-1 was detected throughout the striatum and reached the cerebral cortex at 0.5 h after injection (Figure 6A). Thereafter, GST immunoreactivity gradually decreased until 24 h after injection and was hardly detected at 72 h (Figures 6B and 6C).

To clarify whether exogenous GST-DJ-1 was taken up by neurons and/or glial cells, we performed double staining using antibodies against GST and NeuN, glial fibrillary acidic protein, or CD11b. At 0.5 h after injection, GST immunoreactivity was markedly detected at the extracellular space and in NeuN-immunopositive neurons (Figure 6D). At 3 h after injection, GST immunoreactivity was detected

at the extracellular space and was stronger in NeuN-positive neurons (Figure 6D). Conversely, at 3 h after injection, GST immunoreactivity was partially detected in glial fibrillary acidic protein-immunopositive astrocytes and was scarcely detectable in CD11b-immunopositive microglia (Figure 6D).

### Glutathione *S*-Transferase-Tagged Human DJ-1 Inhibits H₂O₂-Induced Reactive Oxygen Species Production and Cell Death in human SH-SY5Y cells and DJ-1-Knockdown Cells

Recent structural and biochemical analyses have shown that DJ-1 forms a homodimer and that loss of
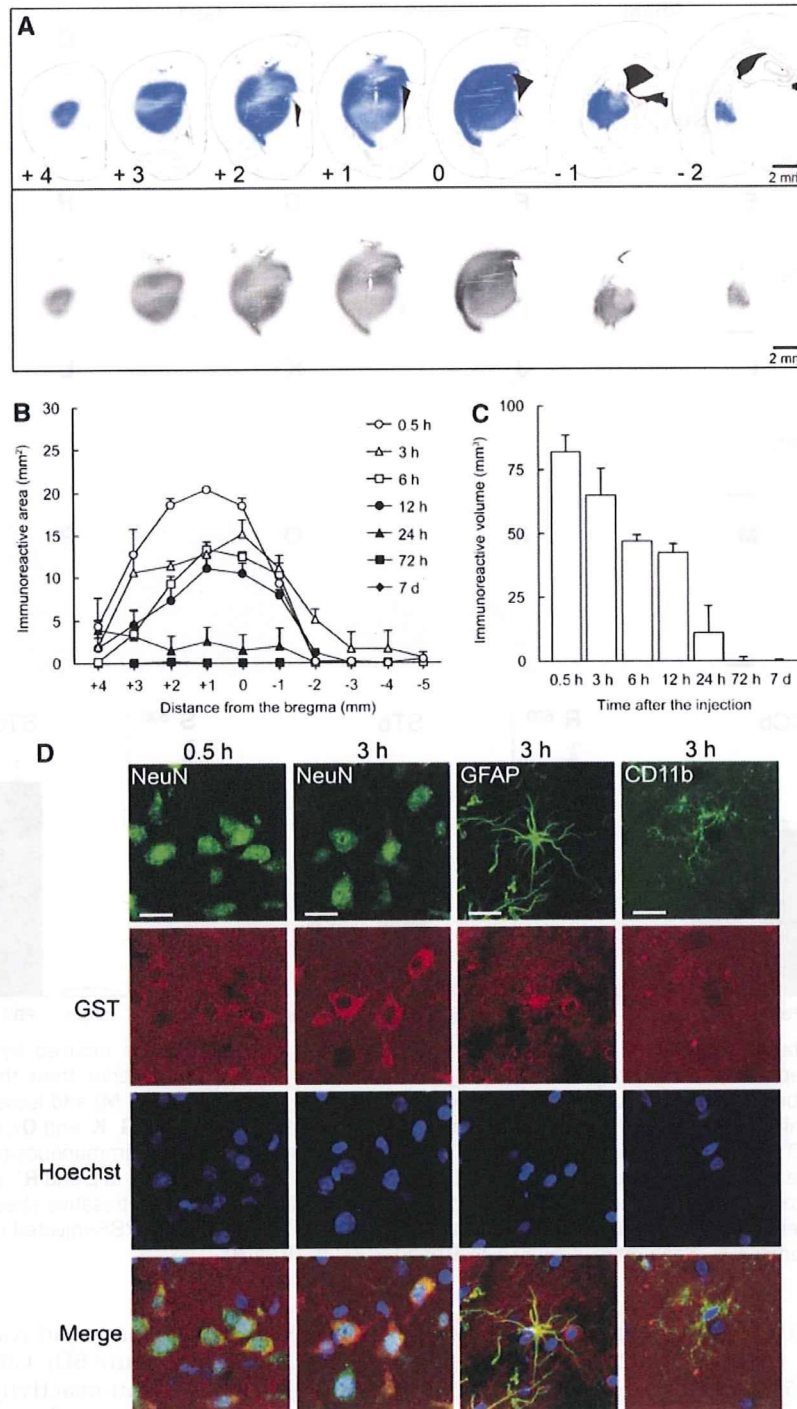
**Figure 6** GST immunoreactivity for exogenous GST-tagged human DJ-1 (GST-DJ-1) in the rat brain. (**A, B**) Schematic diagram of rat coronal brain sections at $+4$, $+3$, $+2$, $+1$, $\pm0$, $-1$, and $-2$ mm anterior–posterior from the bregma. Blue regions with brain map in A indicate GST immunoreactivity, which corresponds to coronal brain sections that were immunostained with anti-GST antibody at 0.5 h after the injection of GST-DJ-1 (320 pmol). (**B, C**) GST-immunoreactive area (**B**) was measured by computerized image analysis, and then GST-immunoreactive volume (**C**) was estimated. $n = 3$ per group. (**D**) Double-immunofluorescence analysis using antibodies against GST for exogenous GST-DJ-1 and NeuN, glial fibrillary acidic protein (GFAP) or CD11b at 0.5 or 3 h after the injection. Data are the mean $\pm$ s.e.m. Scale bars: 2 mm (**A**), 20 $\mu$m (**D**).

574

the homodimer formation of L166P-DJ-1 results in loss of its function (Taira et al, 2004; Takahashi-Niki et al, 2004; Honbou et al, 2003). To investigate whether GST, GST-DJ-1, or GST-L166P-DJ-1 affected the level of ROS production, we performed a confocal analysis with a ROS-specific fluorogen C-DCDHF-DA. $H_2O_2$-induced intracellular C-fluorescence markedly increased when normal human SH-SY5Y cells were treated with 100 $\mu$mol/L $H_2O_2$ for 1 h (Figure 7A).

At that time (after 1 h), $H_2O_2$-induced intracellular ROS production was significantly inhibited by simultaneous treatment with 1 $\mu$mol/L GST-DJ-1 but not by treatment with GST or GST-L166P-DJ-1 (Figures 7A to 7C). Furthermore, after 24 h, $H_2O_2$-induced cell death was also significantly inhibited by 1 $\mu$mol/L GST-DJ-1 but not by GST and GST-L166P-DJ-1 (Figure 7D).

We also established DJ-1-knockdown SH-SY5Y cell line, in which the expression of endogenous human DJ-1 was suppressed by approximately 76% (Figure 8A). In normal SH-SY5Y cells, ROS produc-

tion was induced markedly by 100 $\mu$mol/L $H_2O_2$ (Figure 7), it was induced moderately by 50 $\mu$mol/L $H_2O_2$ (Figures 8B and 8C). In DJ-1-knockdown cells, even 50 $\mu$mol/L $H_2O_2$ induced significant ROS production after 1 h. In addition, massive cell death of DJ-1-knockdown cells was caused by 50 $\mu$mol/L $H_2O_2$ in comparison with normal cells (Figure 8D). $H_2O_2$-induced intracellular ROS production and cell death in DJ-1-knockdown cells were significantly inhibited by GST-DJ-1 (Figures 8C and 8D). In contrast, GST and GST-L166P-DJ-1 had no effect.

## Discussion

Although oxygen is necessary for life, it paradoxically produces ROS, which is highly toxic to cells, as a by-product of its metabolism. Reactive oxygen species is massively produced in the brain after cerebral ischemia and reperfusion. All of these species are redox active and can interact with nearby cellular components, such as proteins,
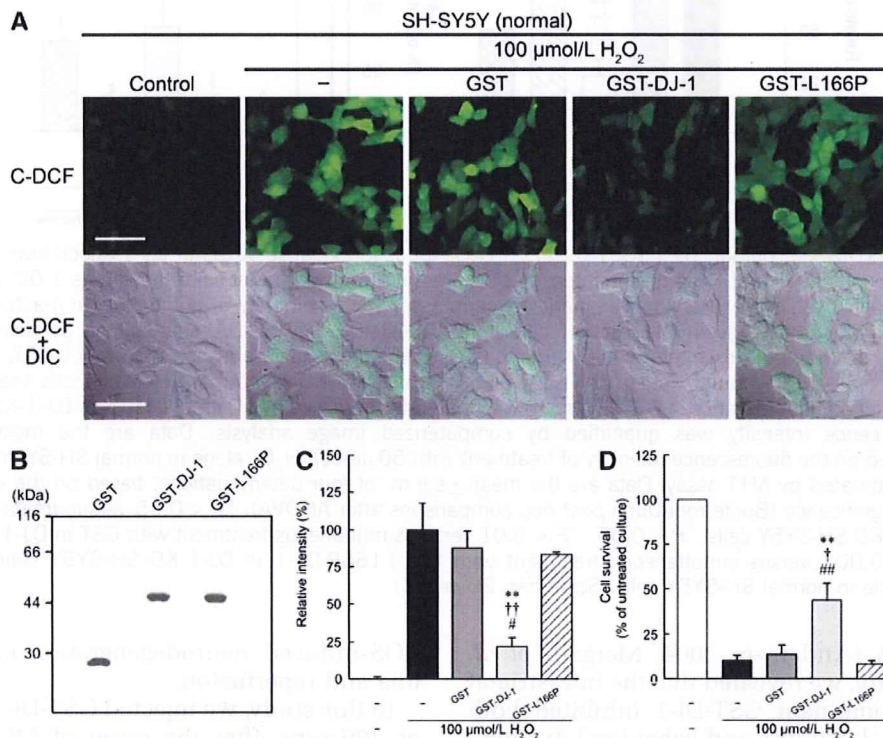


**Figure 7** Effect of GST-tagged human DJ-1 (GST-DJ-1) on $H_2O_2$-induced oxidative stress in normal SH-SY5Y cells. 6-Carboxy-2′,7′-dichlorodihydrofluorescein diacetate di(acetoxymethyl) ester (C-DCDHF-DA) staining was performed at 1 h, and MTT assay for cell survival at 24 h after treatment with 100 $\mu$mol/L $H_2O_2$ in the presence or absence of 1 $\mu$mol/L GST, 1 $\mu$mol/L GST-DJ-1, or 1 $\mu$mol/L GST-tagged L166P-mutant human DJ-1 (GST-L166P). (**A**) Reactive oxygen species production. Fluorescence of C-DCF (green) was markedly increased by 100 $\mu$mol/L $H_2O_2$ (upper row). In contrast, simultaneous treatment with GST-DJ-1 inhibited the increase in fluorescence intensity induced by $H_2O_2$. Cellular images were obtained by the difference interference contrast (DIC; lower row). (**B**) Used recombinant proteins (each 2.5 $\mu$g/lane, stained by Coomassie blue). (**C**) The relative fluorescence intensity was quantified by computerized image analysis. Data are the mean ± s.e.m. of three determinations, based on the fluorescence intensity of treatment with 100 $\mu$mol/L $H_2O_2$ alone as 100%. (**D**) Cell survival was estimated by MTT. Data are the mean ± s.e.m. of four determinations, based on the untreated culture as 100%. Significance (Bonferroni/Dunn post hoc comparisons after ANOVA): **$P < 0.01$ versus treatment with 100 $\mu$mol/L $H_2O_2$ alone. †$P < 0.05$, ††$P < 0.01$ versus simultaneous treatment with GST. #$P < 0.05$, ##$P < 0.01$ versus simultaneous treatment with GST-L166P-DJ-1. Scale bar: 20 $\mu$m (**A**).
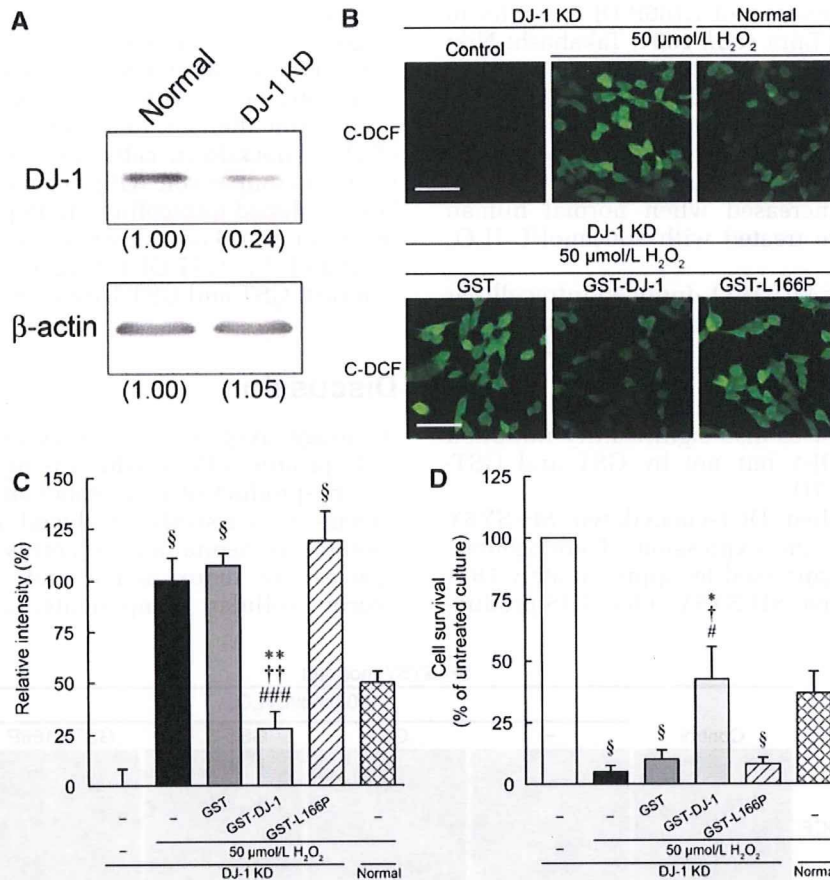
**Figure 8** Effect of GST-tagged human DJ-1 (GST-DJ-1) on $H_2O_2$-induced oxidative stress in DJ-1-knockdown SH-SY5Y cells. (**A**) Expression of endogenous DJ-1 and $\beta$-actin. The intensity of expression level in normal cells showed as 1.00. In DJ-1-knockdown cells (DJ-1-KD), endogenous DJ-1 expression was markedly suppressed (approximately 0.24), but not in $\beta$-actin (1.05). (**B** to **D**) 6-Carboxy-2′,7′-dichlorodihydrofluorescein diacetate di(acetoxymethyl) ester (C-DCDHF-DA) staining was performed at 1 h, and MTT assay for cell survival at 24 h after treatment with 50 $\mu$mol/L $H_2O_2$ in the presence or absence of 1 $\mu$mol/L GST, 1 $\mu$mol/L GST-DJ-1, or 1 $\mu$mol/L GST-tagged L166P-mutant human DJ-1 (GST-L166P) in DJ-1-KD or normal SH-SY5Y cells (normal). (**B**) Reactive oxygen species production. Fluorescence of C-DCF (green) was markedly increased by 50 $\mu$mol/L $H_2O_2$ in DJ-1-KD SH-SY5Y cells (**C**) The relative fluorescence intensity was quantified by computerized image analysis. Data are the mean±s.e.m. of three determinations, based on the fluorescence intensity of treatment with 50 $\mu$mol/L $H_2O_2$ alone in normal SH-SY5Y cells as 100%. (**D**) Cell survival was estimated by MTT assay. Data are the mean±s.e.m. of four determinations, based on the untreated culture as 100%. (**D** and **E**) Significance (Bonferroni/Dunn *post hoc* comparisons after ANOVA): *$P < 0.05$ versus treatment with 50 $\mu$mol/L $H_2O_2$ alone in DJ-1-KD SH-SY5Y cells. †$P < 0.05$, ††$P < 0.01$ versus simultaneous treatment with GST in DJ-1-KD SH-SY5Y cells. #$P < 0.05$, ###$P < 0.001$ versus simultaneous treatment with GST-L166P-DJ-1 in DJ-1-KD SH-SY5Y cells. §$P < 0.05$ versus 50 $\mu$mol/L $H_2O_2$ alone in normal SH-SY5Y cells. Scale bar: 20 $\mu$m (**B**).

lipids, and DNA (Andersen, 2004; Margaill *et al*, 2005). In this study, we revealed that the intrastriatal injection of recombinant GST-DJ-1 inhibited both ischemic neuronal cell loss and behavioral dysfunction induced by 120 mins of MCAO and reperfusion. It has been reported that cells in which endogenous DJ-1 was knocked down or cells which overexpressed point-mutated DJ-1 (such as L166P and C106S) were vulnerable to oxidative stress (Taira *et al*, 2004; Takahashi-Niki *et al*, 2004). More recently, we showed that treatment with GST-DJ-1 protected against nigral dopaminergic neuronal cell death induced by 6-hydroxydopamine-mediated oxidative stress (Inden *et al*, 2006). These observations suggest that the intrastriatal injection of GST-DJ-1 inhibits

ROS-induced neurodegeneration caused by ischemia and reperfusion.

In this study, we injected GST-DJ-1 at 60, 110, 180, or 300 mins after the onset of MCAO. Significant reductions in infarct size were observed when the injection was performed at 60 and 110 mins, and partial reductions were seen at 180 mins, but no reductions in size were seen with the injection at 300 mins. Previous reports have suggested that during 120 mins of MCAO, the levels of 2,3-dihydroxybenzoic acid and 2,5-dihydroxybenzoic acid, as indicators of hydroxyl radicals, increased to values that were 2- to 2.5-fold above baseline and further increased to nearly fourfold at 30 mins after reperfusion (Morimoto *et al*, 1996). Another group

576

reported that a short-lasting increase in lucigenin-enhanced chemiluminescence (an indicator of superoxide production) by nearly fivefold occurred immediately after the initiation of reperfusion in 120 min-MCAO rats (Peters et al, 1998). Moreover, it was reported that the level of NOx (including NOO$^-$ and ONOO$^-$) increased immediately after the onset of reperfusion, and this elevation continued more than 120 mins (Hashiguchi et al, 2003). These observations suggest that ROS production begins to increase gradually after the onset of ischemia, and massively and immediately after reperfusion. Therefore, it seems that when the intrastriatal injection of GST-DJ-1 was performed at 300 mins after the onset of MCAO, ROS production was massively induced, and brain tissue had already been damaged. Furthermore, although exogenous GST-DJ-1 was detected throughout the striatum and partially in the cerebral cortex, the region in which GST-DJ-1 was detected was limited and smaller than the middle cerebral artery-ischemic territory. On the basis of these observations, in the case of intrastriatal injection, the time window of the neuroprotective efficacy of GST-DJ-1 is 110 mins (10 mins before reperfusion) or partially until 180 mins after the onset of MCAO.

In this study, we further performed a noninvasive evaluation of infarct size, using a 7 T Unity Inova MR scanner, and found a reduction in infarct size after the administration of GST-DJ-1. Thus, we suggest that MR imaging is a powerful tool for noninvasive measurement of the extent of ischemic brain injury.

We used a redox-sensitive dye 6-carboxy-2′, 7′-dichlorodihydrofluorescein diacetate di(acetoxymethyl) ester to detect H$_2$O$_2$-mediated ROS production in the in vitro study of human SH-SY5Y cells. Our data showed that GST-DJ-1 reduced intracellular ROS production induced by H$_2$O$_2$ in SH-SY5Y cells. In addition, H$_2$O$_2$-induced ROS production and cell death in SH-SY5Y cells were exacerbated by a knockdown of endogenous human DJ-1 expression. ROS-induced insults were inhibited by GST-DJ-1 but not by GST-L166P-DJ-1 and GST. These results suggest that endogenous DJ-1 may be consumed by the exposure of oxidative stress and that GST-DJ-1 can make up for the lost endogenous DJ-1. However, we showed that exogenous GST-DJ-1 rapidly diffused to the extracellular space in the rat brain, and was readily taken up mainly by neurons and partially by astrocytes. On the basis of these observations, we consider that exogenous GST-DJ-1 has the potential to scavenge both extracellular and intracellular ROS and thereby suppresses ROS-mediated neurodegeneration and exacerbation.

In the immunohistochemical analysis, the formation of nitrotyrosine, which is considered to be a long-lived footprint of NO and ONOO$^-$ (Osuka et al, 2001), was inhibited by the administration of GST-DJ-1. Ischemia/reperfusion injury produces massive amounts of superoxide anion and nitric oxide. Nitric oxide reacts with superoxide anion and is then converted to peroxynitrite, which strongly reacts

with cellular components. When proteins react with peroxynitrite, protein nitration occurs and this results in cellular injury. DJ-1 protein harbors three cysteine residues. It has been shown that DJ-1 forms a homodimer and that Cys106 is selectively oxidized under oxidative stress to eliminate ROS (Canet-Aviles et al, 2004; Honbou et al, 2003; Huai et al, 2003; Kinumi et al, 2004; Taira et al, 2004; Tao and Tong, 2003; Wilson et al, 2003). Furthermore, it has been reported that Cys46 and Cys53, but not Cys106, are susceptible to S-nitrosylation (Ito et al, 2006). Protein S-nitrosylation is a reversible posttranslational modification that targets the thiol group of cysteine residues in proteins by the attack of nitric oxide, which yields more stable S-nitrosocysteine than nitric oxide itself (Ito et al, 2006; Stamler et al, 1992). These findings suggest that DJ-1 reduced the levels of oxidative and nitrosative stress through the modulation of cysteine residues and that this resulted in the inhibition of nitrotyrosine formation induced by cerebral ischemia and reperfusion.

To evaluate a neuroprotective effect of DJ-1, we investigated neural cell injury in the immuno-stained sections. Recently, unbiased stereological technique (such as three-dimensional stereological method) has come to be known a powerful tool with high potential for the counting of critical neural cell numbers in brain sections. However, the aim of this study was to evaluate neural cell injury, but not to determine changes in the critical number of neural cells. Therefore, the number of immunostained neurons was measured using a computerized image analysis based on a two-dimensional morphologic method (Figure 5 and Supplementary Figure S4), which is also one of the applied unbiased methods that is even now widely used for cell counting in damaged tissues (Inden et al, 2006). In this technique, each immunostained neuron is recognized and counted independently to cell size by the computerized image software. It is known that atrophy of the substantia nigra occurs in MCAO rats. In permanent MCAO rats, atrophy did not detect at 1 week, but it markedly occurred at 2 weeks (Tamura et al, 1990). As we performed 2-h MCAO and reperfusion (but not permanent) and immunohistochemical assay at 7 days after MCAO, atrophy in the cerebral cortex, striatum, and substantia nigra was undetectable. Therefore, although the stereological method is now the gold standard to evaluate cell loss, we assessed neuroprotective effect of DJ-1 by a computerized image analysis in this study.

We showed that DJ-1 had a neuroprotective effect against cerebral ischemia and reperfusion in rats. DJ-1 is widely expressed in the human and rodent brain (Bandopadhyay et al, 2004; Olizmann et al, 2007; Yanagida et al, 2006). Furthermore, it has been suggested that DJ-1 plays an important role in systems that defend against oxidative stress (Canet-Aviles et al, 2004; Kinumi et al, 2004; Mitsumoto et al, 2001; Taira et al, 2004). Therefore, it is believed that the development of drugs or treatments that

enhance the expression of endogenous DJ-1 in the brain may be a novel therapeutic strategy in neurodegenerative disorders. Recently, peptide carriers, such as TAT and PEP-1, have been studied with regard to their ability to promote protein transduction not only *in vitro* but also *in vivo* (Denicourt and Dowdy, 2003), and several reports have shown that protein transduction therapy has neuroprotective effects using peptide carriers, such as TAT-Bcl-xL, TAT-GluR6-9c, and PEP-1-SOD, in animal models of cerebral ischemia (Cao *et al*, 2002; Eum *et al*, 2004; Pei *et al*, 2006). These observations suggest that it is possible to deliver DJ-1 protein into brain cells using a peptide carrier to protect against ischemic neurodegeneration. Thus, DJ-1 may be useful in a novel neuroprotective strategy for neurodegenerative disorders, including cerebral ischemia.

In conclusion, this is the first report to show that GST-DJ-1 has a neuroprotective effect in an *in vivo* model of focal cerebral ischemia. Glutathione S-transferase-tagged human DJ-1 protein inhibited ischemic neurodegeneration and ischemia-induced behavioral dysfunction. In addition, we performed a noninvasive analysis using MR imaging to evaluate ischemic size and found a reduction in infarct size with the administration of GST-DJ-1. Nitrotyrosine formation *in vivo*, induced by ischemia/reperfusion injury, was also inhibited by GST-DJ-1. Furthermore, *in vitro* knock down of endogenous DJ-1 expression exacerbated oxidative stress, and GST-DJ-1 protected oxidative insults in SH-SY5Y cells, but did not affect GST and GST-L166P-DJ-1. These results indicate that exogenous GST-DJ-1 plays a neuroprotective role through the reduction of oxidative and nitrosative stress, which suggests that DJ-1 may be useful for the development of novel therapeutic targets in various oxidative and nitrosative stress-mediated disorders including cerebral ischemia.

## Conflict of interest

The authors declare no conflict of interest.

## References

Andersen JK (2004) Oxidative stress in neurodegeneration: cause or consequence? *Nat Med* 10:S18–25

Bandopadhyay R, Kingsbury AE, Cookson MR, Reid AR, Evans IM, Hope AD, Pittman AM, Lashley T, Canet-Aviles R, Miller DW, McLendon C, Strand C, Leonard AJ, Abou-Sleiman PM, Healy DG, Ariga H, Wood NW, de Silva R, Revesz T, Hardy JA, Lees AJ (2004) The expression of DJ-1 (PARK7) in normal human CNS and idiopathic Parkinson's disease. *Brain* 127:420–30

Bederson JB, Pitts LH, Tsuji M, Nishimura MC, Davis RL, Bartkowski H (1986) Rat middle cerebral artery occlusion: evaluation of the model and development of a neurologic examination. *Stroke* 17:472–6

Bonifati V, Rizzu P, van Baren MJ, Schaap O, Breedveld GJ, Krieger E, Dekker MC, Squitieri F, Ibanez P, Joosse M, van Dongen JW, Vanacore N, van Swieten JC, Brice A, Meco G, van Duijn CM, Oostra BA, Heutink P (2003)

Mutations in the *DJ-1* gene associated with autosomal recessive early-onset Parkinsonism. *Science* 299:256–9

Canet-Aviles RM, Wilson MA, Miller DW, Ahmad R, McLendon C, Bandyopadhyay S, Baptista MJ, Ringe D, Petsko GA, Cookson MR (2004) The Parkinson's disease protein DJ-1 is neuroprotective due to cysteine-sulfinic acid-driven mitochondrial localization. *Proc Natl Acad Sci USA* 101:9103–8

Cao G, Pei W, Ge H, Liang Q, Luo Y, Sharp FR, Lu A, Ran R, Graham SH, Chen J (2002) In vivo delivery of a Bcl-xL fusion protein containing the TAT protein transduction domain protects against ischemic brain injury and apoptosis. *J Neurosci* 22:5423–31

Chen L, Cagniard B, Mathews T, Jones S, Koh HC, Ding Y, Carvey PM, Ling Z, Kang UJ, Zhuang X (2005) Age-dependent motor deficits and dopaminergic dysfunction in DJ-1 null mice. *J Biol Chem* 280:21418–26

Denicourt C, Dowdy SF (2003) Protein transduction technology offers novel therapeutic approach for brain ischemia. *Trends Pharmacol Sci* 24:216–8

Eum WS, Kim DW, Hwang IK, Yoo KY, Kang TC, Jang SH, Choi HS, Choi SH, Kim YH, Kim SY, Kwon HY, Kang JH, Kwon OS, Cho SW, Lee KS, Park J, Won MH, Choi SY (2004) In vivo protein transduction: biologically active intact PEP-1-superoxide dismutase fusion protein efficiently protects against ischemic insult. *Free Radic Biol Med* 37:1656–69

Gao Y, Signore AP, Yin W, Cao G, Yin XM, Sun F, Luo Y, Graham SH, Chen J (2005) Neuroprotection against focal ischemic brain injury by inhibition of c-Jun N-terminal kinase and attenuation of the mitochondrial apoptosis-signaling pathway. *J Cereb Blood Flow Metab* 25:694–712

Goldberg MS, Pisani A, Haburcak M, Vortherms TA, Kitada T, Costa C, Tong Y, Martella G, Tscherter A, Martins A, Bernardi G, Roth BL, Pothos EN, Calabresi P, Shen J (2005) Nigrostriatal dopaminergic deficits and hypokinesia caused by inactivation of the familial Parkinsonism-linked gene DJ-1. *Neuron* 45:489–96

Hashiguchi A, Kawano T, Yano S, Morioka M, Handa J, Sato T, Shirasaki Y, Ushio Y, Fukunaga K (2003) The neuroprotective effect of a novel calmodulin antagonist, 3-[2-[4-(3-chloro-2-methylphenyl)-1-piperazinyl]-ethyl]-5,6-dimethoxy-1-(4-imidazolylmethyl)-1H-indazole dihydrochloride 3.5 hydrate, in transient forebrain ischemia. *Neuroscience* 121:379–86

Hata R, Maeda K, Hermann D, Mies G, Hossmann KA (2000) Evolution of brain infarction after transient focal cerebral ischemia in mice. *J Cereb Blood Flow Metab* 20:937–46

Honbou K, Suzuki NN, Horiuchi M, Niki T, Taira T, Ariga H, Inagaki F (2003) The crystal structure of DJ-1, a protein related to male fertility and Parkinson's disease. *J Biol Chem* 278:31380–4

Huai Q, Sun Y, Wang H, Chin LS, Li L, Robinson H, Ke H (2003) Crystal structure of DJ-1/RS and implication on familial Parkinson's disease. *FEBS Lett* 549:171–5

Inden M, Taira T, Kitamura Y, Yanagida T, Tsuchiya D, Takata K, Yanagisawa D, Nishimura K, Taniguchi T, Kiso Y, Yoshimoto K, Agatsuma T, Koide-Yoshida S, Iguchi-Ariga SMM, Shimohama S, Ariga H (2006) PARK 7 DJ-1 protects against degeneration of nigral dopaminergic neurons in Parkinson's disease rat model. *Neurobiol Dis* 24:144–58

Ito G, Ariga H, Nakagawa Y, Iwatsubo T (2006) Roles of distinct cysteine residues in S-nitrosylation and dimerization of DJ-1. *Biochem Biophys Res Commun* 339:667–72

578

Jin J, Meredith GE, Chen L, Zhou Z, Xu J, Shie FS, Lockhart P, Zhang J (2005) Quantitative proteomic analysis of mitochondrial proteins: relevance to Lewy body formation and Parkinson's disease. *Mol Brain Res* 143:119–38

Kim RH, Smith PD, Aleyasin H, Hayley S, Mount MP, Pownall S, Wakeham A, You-Ten AJ, Kalia SK, Horne P, Westaway D, Lozano AM, Anisman H, Park DS, Mak TW (2005) Hypersensitivity of DJ-1-deficient mice to 1-methyl-4-phenyl-1,2,3,6-tetrahydropyrindine (MPTP) and oxidative stress. *Proc Natl Acad Sci USA* 102: 5215–5220

Kinumi T, Kimata J, Taira T, Ariga H, Niki E (2004) Cysteine-106 of DJ-1 is the most sensitive cysteine residue to hydrogen peroxide-mediated oxidation *in vivo* in human umbilical vein endothelial cells. *Biochem Biophys Res Commun* 317:722–8

Kitamura Y, Kosaka T, Kakimura JI, Matsuoka Y, Kohno Y, Nomura Y, Taniguchi T (1998) Protective effects of the antiparkinsonian drugs talipexole and pramipexole against 1-methyl-4-phenylpyridinium-induced apoptotic death in human neuroblastoma SH-SY5Y cells. *Mol Pharmacol* 54:1046–54

Kitamura Y, Yanagisawa D, Inden M, Takata K, Tsuchiya D, Kawasaki T, Taniguchi T, Shimohama S (2005) Recovery of focal brain ischemia-induced behavioral dysfunction by intracerebroventricular injection of microglia. *J Pharmacol Sci* 97:289–93

Lin TN, He YY, Wu G, Khan M, Hsu CY (1993) Effect of brain edema on infarct volume in a focal cerebral ischemia model in rats. *Stroke* 24:117–21

Margaill I, Plotkine M, Lerouet D (2005) Antioxidant strategies in the treatment of stroke. *Free Radic Biol Med* 39:429–43

Mitsumoto A, Nakagawa Y, Takeuchi A, Okawa K, Iwamatsu A, Takanezawa Y (2001) Oxidized forms of peroxiredoxins and DJ-1 on two-dimensional gels increased in response to sublethal levels of paraquat. *Free Radic Res* 35:301–10

Morimoto T, Globus MYT, Busto R, Martinez E, Ginsberg MD (1996) Simultaneous measurement of salicylate hydroxylation and glutamate release in the penumbral cortex following transient middle cerebral artery occlusion in rats. *J Cereb Blood Flow Metab* 16:92–9

Nagakubo D, Taira T, Kitaura H, Ikeda M, Tamai K, Iguchi-Ariga SMM, Ariga H (1997) DJ-1, a novel oncogene which transforms mouse NIH3T3 cells in cooperation with ras. *Biochem Biophys Res Commun* 231:509–13

Nagasawa H, Kogure K (1989) Correlation between cerebral blood flow and histologic changes in a new rat model of middle cerebral artery occlusion. *Stroke* 20:1037–43

Niki T, Takahashi-Niki K, Taira T, Iguchi-Ariga SMM, Ariga H (2003) DJBP: a novel DJ-1-binding protein, negatively regulates the androgen receptor by recruiting histone deacetylase complex, and DJ-1 antagonizes this inhibition by abrogation of this complex. *Mol Cancer Res* 1:247–61

Olizmann JA, Bordelon JR, Muly EC, Rees HD, Levey AI, Li L, Chin LS (2007) Selective enrichment of DJ-1 protein in primate striate neuronal processes: implications for Parkinson's disease. *J Comp Neurol* 500: 585–599

Osuka K, Feustel PJ, Mongin AA, Tranmer BI, Kimelberg HK (2001) Tamoxifen inhibits nitrotyrosine formation after reversible middle cerebral artery occlusion in the rat. *J Neurochem* 76:1842–50

Paxinos G, Watson C (eds) (2005) *The rat brain in stereotaxic coordinates* 5th ed. Burlington, London: Elsevier Academic Press

Pei DS, Wang XT, Liu Y, Sun YF, Guan QH, Wang W, Yan JZ, Zong YY, Xu TL, Zang GY (2006) Neuroprotection against ischemic brain injury by a GluR6-9c peptide containing the TAT protein transduction sequence. *Brain* 129:465–79

Peters O, Back T, Lindauer U, Busch C, Megow D, Dreier J, Dirnagi U (1998) Increased formation of reactive oxygen species after permanent and reversible middle cerebral artery occlusion in the rat. *J Cereb Blood Flow Metab* 18:196–205

Shendelman S, Jonason A, Martinat C, Leete T, Abeliovich A (2004) DJ-1 is a redox-dependent molecular chaperone that inhibits alpha-synuclein aggregate formation. *PloS Biol* 2:1764–73

Shinbo Y, Taira T, Niki T, Iguchi-Ariga SMM, Ariga H (2005) DJ-1-restores p53 transcription activity inhibited by Topors/p53BP3. *Int J Oncol* 26:641–8

Stamler JS, Simon DI, Osborne JA, Mullins M, Jaraki O, Michel T, Singel DJ, Loscalzo J (1992) S-nitrosylation of proteins with nitric oxide: synthesis and characterization of biologically active compounds. *Proc Natl Acad Sci USA* 89:444–8

Swanson RA, Morton MT, Tsao-Wu G, Savalos RA, Davidson CD, Sharp FR (1989) A semiautomated method for measuring brain infarct volume. *J Cereb Blood Flow Metab* 10:290–3

Suzuki S, Yamashita T, Tanaka K, Hattori H, Sawamoto K, Okano H, Suzuki N (2005) Activation of cytokine signaling through leukemia inhibitory factor receptor (LIFR)/gp130 attenuates ischemic brain injury in rats. *J Cereb Blood Flow Metab* 25:685–93

Taira T, Saito Y, Niki T, Iguchi-Ariga SMM, Takahashi K, Ariga H (2004) DJ-1 has a role in antioxidative stress to prevent cell death. *EMBO Rep* 5:213–8

Takahashi K, Taira T, Niki T, Seino C, Iguchi-Ariga SMM, Ariga H (2001) DJ-1 positive regulates the androgen receptor by impairing the binding of PIASx alpha to the receptor. *J Biol Chem* 276:37556–63

Takahashi-Niki K, Niki T, Taira T, Iguchi-Ariga SMM, Ariga H (2004) Reduced anti-oxidative stress activities of DJ-1 mutants found in Parkinson's disease patients. *Biochem Biophys Res Commun* 320:389–97

Tamura A, Kirino T, Sano K, Takagi K, Oka H (1990) Atrophy of the ipsilateral substantia nigra following middle cerebral artery occlusion in the rat. *Brain Res* 510:154–7

Tao X, Tong L (2003) Crystal structure of human DJ-1, a protein associated with early-onset Parkinson's disease. *J Biol Chem* 278:31372–9

Wilson MA, Collins JL, Hod Y, Ringe D, Petsko GA (2003) The 1.1-A resolution crystal structure of DJ-1, the protein mutated in autosomal recessive early onset Parkinson's disease. *Proc Natl Acad Sci USA* 100: 9256–9261

Yanagida T, Takata K, Inden M, Kitamura Y, Taniguchi T, Yoshimoto K, Taira T, Ariga H (2006) Distribution of DJ-1, Parkinson's disease-related protein PARK7, and its alteration in 6-hydroxydopamine-treated hemiparkinsonian rat brain. *J Pharmacol Sci* 102:243–7

Supplementary Information accompanies the paper on the Journal of Cerebral Blood Flow & Metabolism website (http://www.nature.com/jcbfm)

# Preparation of Fluorescent Diamond Nanoparticles Stably Dispersed under a Physiological Environment through Multistep Organic Transformations

Tatsuya Takimoto,[†] Tokuhiro Chano,[‡] Sawako Shimizu,[‡] Hidetoshi Okabe,[‡] Masaaki Ito,[§]
Masahito Morita,[⊥,#] Takahide Kimura,[†] Toshiro Inubushi,[‖] and Naoki Komatsu*,[†]

[†]*Department of Chemistry, Shiga University of Medical Science, Seta, Otsu 520-2192, Japan,* [‡]*Department
of Clinical Laboratory Medicine, Shiga University of Medical Science, Seta, Otsu 520-2192, Japan,* [§]*Organic
Chemical Company, Daicel Chemical Industries, Ltd., 2-1-4 Higashisakae, Ohtake, Hiroshima 739-0605,
Japan,* [⊥]*Immunology Frontier Research Center, Osaka University, 3-1 Yamadaoka, Suita 565-0871, Japan,*
[#]*PRESTO, JST, 4-1-8, Honcho, Kawaguchi-shi, Saitama, 332-0012, Japan, and* [‖]*Biomedical MR Science Center,
Shiga University of Medical Science, Seta, Otsu 520-2192, Japan*

Received February 24, 2010. Revised Manuscript Received April 8, 2010

Imparting multiple functions to nanoparticles through organic functionalization has been attracting significant interest, particularly in terms of biomedical applications. Among them, diamond nanoparticles—the so-called nanodiamond (ND)—have been recognized as one of the best platforms, because of its nontoxic or low-toxicity properties, as well as its organic characteristics that enable covalent bonding with introduced functionalities. Here, we show multistep organic transformations on the ND surface that amass the requisite functions layer by layer through covalent bonds. The functionalities introduced onto the ND surface were well-characterized by solution-phase $^1$H NMR and $^{13}$C NMR spectroscopies, recently developed by us and other groups, as well as conventional infrared (IR), fluorescence microscopy and spectroscopy, and elemental analysis. As a result, hydrophilic and fluorescent characteristics were incorporated onto the ND surface by adding polyethylene glycol (PEG) and fluorescein segments, providing fluorescent ND stably dispersed under a physiological environment. ND has been confirmed to be viable for use as a cellular imaging agent by introducing them into HeLa cells.

## Introduction

Biomedical applications of nanoparticles have attracted growing interest, because of the high potential for early diagnosis and targeted therapeutics.[1−8] In particular, various inorganic nanoparticles made from gold, silica, iron oxide, manganese oxide, and cadmium selenide (quantum dots) are frequently used as platforms for biomedical imaging[9] or drug delivery,[10,11] mainly because

of the availability of the size-controlled particles,[12−14] and/or their characteristic magnetic and optical properties.[15−17] However, in view of their clinical use, more functions should be programmed into the nanoparticles, such as in vivo dispersibility, target specificity, controlled release, and multiple imaging modalities. Therefore, appropriate organic functionalities are frequently required to be immobilized on the surface of the nanoparticles to add more and tunable functions for nanoparticles. However, methods of chemical functionalization onto the inorganic (noncarbonaceous) nanoparticles are limited; reliable methods to construct the interfacial connections between inorganic core and organic functionalities have been confined mostly to sol−gel reactions of silica nanoparticles,[18] lipid coating of

*Author to whom correspondence should be addressed. Tel.: +81-77-548-2102. Fax: +81-77-548-2405. E-mail address: nkomatsu@belle.shiga-med.ac.jp.

(1) De, M.; Ghosh, P. S.; Rotello, V. M. *Adv. Mater.* 2008, *20*, 4225–4241.
(2) Rao, J. *ACS Nano* 2008, *2*, 1984–1986.
(3) Emerrich, D. F.; Thanos, C. G. *J. Drug Targeting* 2007, *15*, 163–183.
(4) Caruthers, S. D.; Wickline, S. A.; Lanza, G. M. *Curr. Opin. Biotechnol.* 2007, *18*, 26–30.
(5) Farokhzad, O. C.; Langer, R. *Adv. Drug Delivery Rev.* 2006, *58*, 1456–1459.
(6) Gil, P. R.; Parak, W. J. *ACS Nano* 2008, *2*, 2200–2205.
(7) Liu, Y.; Miyoshi, H.; Nakamura, M. *Int. J. Cancer* 2007, *120*, 2527–2537.
(8) Jain, K. K. *Clin. Chim. Acta* 2005, *358*, 37–54.
(9) Cheon, J.; Lee, J.-H. *Acc. Chem. Res.* 2008, *41*, 1630–1640.
(10) Farokhzad, O. C.; Langer, R. *ACS Nano* 2009, *3*, 16–20.
(11) Peer, D.; Karp, J. M.; Hong, S.; Farokhzad, O. C.; Margalit, R.; Langer, R. *Nature Nanotechnol.* 2007, *2*, 751–760.
(12) Tao, A. R.; Habas, S.; Yang, P. *Small* 2008, *4*, 310–325.

(13) Skrabalak, S. E.; Xia, Y. *ACS Nano* 2009, *3*, 10–15.
(14) Zhang, Q.; Xie, J.; Yang, J.-H.; Lee, J. Y. *ACS Nano* 2009, *3*, 139–148.
(15) Cai, W.; Chen, X. *Small* 2007, *3*, 1840–1854.
(16) Douma, K.; Prinzen, L.; Slaaf, D. W.; Reutelingsperger, C. P. M.; Biessen, E. A. L.; Hackeng, T. M.; Post, M. J.; van Zandvoort, M. A. M. J. *Small* 2009, *5*, 544–557.
(17) Rogach, A. L.; Gaponik, N.; Lupton, J. M.; Bertoni, C.; Gallardo, D. E.; Dunn, S.; Pira, N. L.; Paderi, M.; Repetto, P.; Romanov, S. G.; O'Dwyer, C.; Torres, C. M. S.; Eychmüller, A. *Angew. Chem., Int. Ed.* 2008, *47*, 6538–6549.
(18) Jamieson, T.; Bakhshi, R.; Petrova, D.; Pocock, R.; Imani, M.; Seifalian, A. M. *Biomaterials* 2007, *28*, 4717–4732.

hydrophobic nanoparticles,[19] and ligation of thiol to metallic nanoparticles.[20]

In contrast, carbon nanomaterials such as carbon nanotubes, fullerenes, and, quite recently, nanographene have been functionalized covalently in various ways, thanks to their organic characteristics.[21-23] Although carbon materials are classified as inorganic, their behaviors toward organic functionalization are different from noncarbonaceous materials. Diamond is also categorized as an inorganic material, because of its robustness and chemical stability. Many organic reactions have been applied to form covalent bonds between the diamond surface and the functionalities[24-27] both in film[28-36] and nanometer-sized particles.[37-45] The chemically inert but functionalizable characteristics of diamond have been recently applied to the synthesis of diamond-based biosensors[32] and DNA chips.[31,33,46] Diamond has gradually taken on organic characteristics, as well as fullerenes and carbon nanotubes.[47]

Diamond nanoparticles—the so-called nanodiamond (ND)—have been recently attracting significant interest in their biological and medicinal applications, mainly because of their nontoxic or low-toxicity properties, as well as their above-mentioned organic characteristics. Various types of fluorescent ND have already been prepared physically by ion implantation[48-56] and chemically by organic functionalization,[57-60] and they have been introduced into cells, exhibiting almost no cytotoxicity. However, NDs (~50 and 5 nm in size) have been reported to form unstable hydrosols without the aid of a surfactant and precipitate under a physiological environment (for example, in phosphate buffer saline (PBS)).[59,61,62] We also have observed similar phenomena, as will be mentioned below (Figure 7). In view of further extensions of the biomedical applications, a stable hydrosol of ND should be produced by surface modification, as noted in the review articles recently written by Shenderova[61] and Dai.[63] In addition, an increasing number of excellent papers have appeared in recent years on the subject of covalent chemical functionalization and characterization of NDs,[50,57,59,60,64-67] which has prompted us to report our results.

(19) van Schooneveld, M. M.; Vucic, E.; Koole, R.; Zhou, Y.; Stocks, J.; Cormode, D. P.; Tang, C. Y.; Gordon, R. E.; Nicolay, K.; Meijerink, A.; Fayad, Z. A.; Mulder, W. J. M. *Nano Lett.* **2008**, *8*, 2517–2525.
(20) Templeton, A. C.; Wuelfing, W. P.; Murray, R. W. *Acc. Chem. Res.* **2000**, *33*, 27–36.
(21) Peng, X.; Wong, S. S. *Adv. Mater.* **2009**, *21*, 625–642.
(22) Liu, Z.; Robinson, J. T.; Sun, X.; Dai, H. *J. Am. Chem. Soc.* **2008**, *130*, 10876–10877.
(23) Liu, Z.; Sun, X.; Nakayama-Ratchford, N.; Dai, H. *ACS Nano* **2007**, *1*, 50–56.
(24) Krueger, A. *Chem.—Eur. J.* **2008**, *14*, 1382–1390.
(25) Krueger, A. *Adv. Mater.* **2008**, *20*, 2445–2449.
(26) Krueger, A. *J. Mater. Chem.* **2008**, *18*, 1485–1492.
(27) Holt, K. B. *Philos. Trans. R. Soc. A* **2007**, *365*, 2845–2861.
(28) Nebel, C. E.; Shin, D.; Rezek, B.; Tokuda, N.; Uetsuka, H.; Watanabe, H. *J. R. Soc. Interface* **2007**, *4*, 439–461.
(29) Zhong, Y. L.; Loh, K. P.; Midya, A.; Chen, Z.-K. *Chem. Mater.* **2008**, *20*, 3137–3144.
(30) Rezek, B.; Shin, D.; Nakamura, T.; Nebel, C. E. *J. Am. Che. Soc.* **2006**, *128*, 3884–3885.
(31) Kuga, S.; Yang, J.-H.; Takahashi, H.; Hirama, K.; Iwasaki, T.; Kawarada, H. *J. Am. Chem. Soc.* **2008**, *130*, 13251–13263.
(32) Härtl, A.; Schmich, E.; Garrido, J. A.; Hernando, J.; Catharino, S. C. R.; Walter, S.; Feulner, P.; Kromka, A.; Steinmüller, D.; Stutzmann, M. *Nat. Mater.* **2004**, *3*, 736–742.
(33) Yang, W.; Auciello, O.; Butler, J. E.; Cai, W.; Carlisle, J. A.; Gerbi, J.; Gruen, D. M.; Knickerbocker, T.; Lasseter, T.; Russell, J. N., Jr.; Smith, L. M.; Hamers, R. J. *Nat. Mater.* **2002**, *1*, 253–257.
(34) Smentkowski, V. S.; Yates, J. T., Jr. *Science* **1996**, *271*, 193–195.
(35) Nakamura, T.; Suzuki, M.; Ishihara, M.; Ohana, T.; Tanaka, A.; Koga, Y. *Langmuir* **2004**, *20*, 5846–5849.
(36) Hovis, J. S.; Coulter, S. K.; Harmers, R. J. *J. Am. Chem. Soc.* **2000**, *122*, 732–733.
(37) Nakamura, T.; Ishihara, M.; Ohana, T.; Koga, Y. *Chem. Commun.* **2003**, 900–901.
(38) Li, L.; Davidson, J. L.; Lukehart, C. M. *Carbon* **2006**, *44*, 2308–2315.
(39) Liu, Y.; Gu, Z.; Margrave, J. L.; Khabashesku, V. N. *Chem. Mater.* **2004**, *16*, 3924–3930.
(40) Miller, J. B.; Brown, D. W. *Langmuir* **1996**, *12*, 5809–5817.
(41) Saito, T.; Ikeda, Y.; Egawa, S.; Kusakabe, K.; Morooka, S.; Maeda, H.; Taniguchi, Y.; Fujiwara, Y. *J. Chem. Soc. Faraday Trans.* **1998**, *94*, 929–932.
(42) Ushizawa, K.; Sato, Y.; Mitsumori, T.; Machinami, T.; Ueda, T.; Ando, T. *Chem. Phys. Lett.* **2002**, *351*, 105–108.
(43) Tsubota, T.; Urabe, K.; Egawa, S.; Takagi, H.; Kusakabe, K.; Morooka, S.; Maeda, H. *Diamond Relat. Mater.* **2000**, *9*, 219–223.
(44) Tsubota, T.; Tanii, S.; Ida, S.; Nagata, M.; Matsumoto, Y. *Phys. Chem. Chem. Phys.* **2003**, *5*, 1474–1480.
(45) Tsubota, T.; Hirabayashi, O.; Ida, S.; Nagaoka, G.; Nagata, M.; Matsumoto, Y. *Phys. Chem. Chem. Phys.* **2002**, *4*, 806–811.
(46) Yang, N.; Uetsuka, H.; Osawa, E.; Nebel, C. E. *Angew. Chem., Int. Ed.* **2008**, *47*, 5183–5185.
(47) Schwertfeger, H.; Fokin, A. A.; Schreiner, P. R. *Angew. Chem., Int. Ed.* **2008**, *47*, 1022–1036.

(48) Vaijayanthimala, V.; Chang, H.-C. *Nanomedicine* **2009**, *4*, 47–55.
(49) Mohan, N.; Tzeng, Y.-K.; Yang, L.; Chen, Y.-Y.; Hui, Y. Y.; Fang, C.-Y.; Chang, H.-C. *Adv. Mater.* **2010**, *22*, 843–847.
(50) Zhang, B.; Li, Y.; Fang, C.-Y.; Chang, C.-C.; Chen, C.-S.; Chen, Y.-Y.; Chang, H.-C. *Small* **2009**, *5*, 2716–2721.
(51) Chang, Y.-R.; Lee, H.-Y.; Chen, K.; Chang, C.-C.; Tsai, D.-S.; Fu, C.-C.; Lim, T.-S.; Tzeng, Y.-K.; Fang, C.-Y.; Han, C.-C.; Chang, H.-C.; Fann, W. *Nature Nanotechnol.* **2008**, *3*, 284–288.
(52) Tisler, J.; Balasubramanian, G.; Naydenov, B.; Kolesov, R.; Grotz, B.; Reuter, R.; Boudou, J. P.; Curmi, P. A.; Sennour, M.; Thorel, A.; Börsch, M.; Aulenbacher, K.; Erdmann, R.; Hemmer, P. R.; Jelezko, F.; Wrachtrup, J. *ACS Nano* **2009**, *3*, 1959–1965.
(53) Faklaris, O.; Joshi, V.; Irinopoulou, T.; Tauc, P.; Sennour, M.; Girard, H.; Gesset, C.; Arnault, J.-C.; Thorel, A.; Boudou, J. P.; Curmi, P. A.; Treussart, F. *ACS Nano* **2009**, *3*, 3955–3962.
(54) Faklaris, O.; Garrot, D.; Joshi, V.; Druon, F.; Boudou, J.-P.; Sauvage, T.; Georges, P.; Curmi, P. A.; Treussart, F. *Small* **2008**, *4*, 2236–2239.
(55) Chang, I. P.; Hwang, K. C.; Chiang, C.-S. *J. Am. Chem. Soc.* **2008**, *130*, 15476–15481.
(56) Chao, J.-I.; Perevedentseva, E.; Chung, P.-H.; Liu, K.-K.; Cheng, C.-Y.; Chang, C.-C.; Cheng, C.-L. *Biophys. J.* **2007**, *93*, 2199–2208.
(57) Martin, R.; Alvaro, M.; Herance, J. R.; Garcia, H. *ACS Nano* **2010**, *4*, 65–74.
(58) Loh, O.; Lam, R.; Chen, M.; Moldovan, N.; Huang, H.; Ho, D.; Espinosa, H. D. *Small* **2009**, *5*, 1667–1674.
(59) Hens, S. C.; Cunningham, G.; Tyler, T.; Moseenkov, S.; Kuznetsov, V.; Shenderova, O. *Diamond Relat. Mater.* **2008**, *17*, 1858–1866.
(60) Vial, S.; Mansuy, C.; Sagan, S.; Irinopoulou, T.; Burlina, F.; Boudou, J. P.; Chassaing, G.; Lavielle, S. *ChemBioChem* **2008**, *9*, 2113–2119.
(61) Schrand, A. M.; Hens, S. A. C.; Shenderova, O. A. *Crit. Rev. Solid State Mater. Sci.* **2009**, *34*, 18–74.
(62) Pyzyr, A. P.; Bondar, V. S.; Bukayemsky, A. A.; Selyutin, G. E.; Kargin, V. F. In *Synthesis, Properties and Applications of Ultrananocrystalline Diamond*; Gruen, D. M., Shenderova, O. A., Vul', A. Y., Eds.; NATO Science Series II Mathematics, Physics and Chemistry; Springer: Dordrecht, The Netherlands, 2005; pp 261–270.
(63) Xing, Y.; Dai, L. *Nanomedicine* **2009**, *4*, 207–218.
(64) Martin, R.; Heydorn, P. C.; Alvaro, M.; Garcia, H. *Chem. Mater.* **2009**, *21*, 4505–4514.
(65) Mochalin, V. N.; Gogotsi, Y. *J. Am. Chem. Soc.* **2009**, *131*, 4594–4595.
(66) Yeap, W. S.; Tan, Y. Y.; Loh, K. P. *Anal. Chem.* **2008**, *80*, 4659–4665.
(67) Cheng, J.; He, J.; Li, C.; Yang, Y. *Chem. Mater.* **2008**, *20*, 4224–4230.
(68) Komatsu, N. *J. Incl. Phenom. Macrocycl. Chem.* **2008**, *61*, 195–216.
(69) Peng, X.; Komatsu, N.; Kimura, T.; Ōsuka, A. *ACS Nano* **2008**, *2*, 2045–2050.

**Scheme 1. Synthetic Route from Hydrogenated ND 1 to Fluorescent ND 3**



**Scheme 2. Synthesis of Nanodiamondyl Aminododecanoate 6 from 1 via Routes A and B**
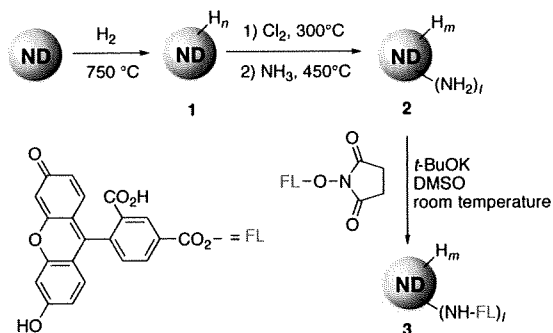


In continuation of our effort to apply organic chemistry to carbon nanomaterials,[68−72] we conducted multistep organic transformations on an ND surface to impart hydrophilic and fluorescent characteristics one by one. In each step of the functionalizations, the product was characterized primarily with solution-phase $^1$H NMR and $^{13}$C NMR spectroscopies, as well as infrared (IR), elemental analysis, and fluorescence microscopy and spectroscopy. The solution-phase NMR technique is much more convenient and informative than a solid-phase one. It is a novel method for analyzing suspended nanoparticles and is found to be applicable to relatively large sizes of nanoparticles (~30 nm).[38,64,72,73] Eventually, we synthesized fluorescent ND that was stably dispersed under a physiological environment and applied it to fluorescence cell imaging.

## Results and Discussion

Since the labeling agents are frequently bound to biological entities through amide linkage by reaction of primary amine with carboxylic acid or its derivatives, we attempted to prepare fluorescent ND 3 from hydrogenated ND 1 via amino-functionalized ND 2, as shown in Scheme 1.[74,75] Although various reaction conditions were examined for the incorporation of fluorescein to 2 through amide linkage, no clear fluorescence was observed from the product 3, as shown in the fluorescence image (see Figure S1a in the Supporting Information), and almost no difference on the IR spectra was observed between 2 and 3 (see Figure S1b in the Supporting Information). These results indicate that little or no fluorescein was introduced to the ND. This may be attributed to steric hindrance on the ND surface, to prevent fluorescein from approaching to the amino groups. Therefore, we designed another precursor
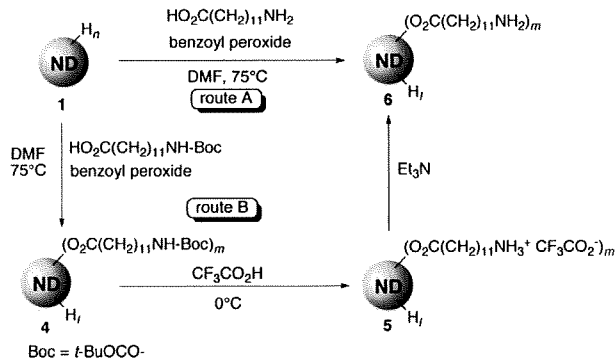
for fluorescent ND that possesses amino groups apart from the ND surface, which fluorescein can freely access.

While nonblinking and nonbleaching fluorescence from ND has been prepared by ion implantation and utilized extensively for cell labeling,[48,50−56] fluorophore-immobilized ND is considered to possess the following advantages: (i) specific instrumentation for ion implantation is not required to make the ND fluoresce, and (ii) emission and excitation wavelengths can be tuned by choosing an appropriate fluorophore.[57,61]

**Synthesis and Characterization of Aminododecanoate of ND.** A radical reaction of hydrogenated ND with carboxylic acid was chosen to bind ω-amino acid on 1 through ester linkage (see Scheme 2).[44,45] We chose this reaction for the following two reasons:

(1) The very simple structure of 1, which consists solely of C (sp$^3$) and H atoms connected by single bonds (C−C and C−H), facilitates the characterization of the product in each step of the organic transformations by IR (Figure 1),[74] NMR (Figure 2),[72] and elemental analysis (Table 1).

(2) The hydrogen-terminated surface in 1 can largely reduce the possibility of physisorption of the reactants onto the ND surface.[76]

In addition to the direct route to 6 through the reaction of ω-aminododecanoic acid with 1 (route A in Scheme 2), Boc (*t*-butoxycarbonyl)-protected ω-aminododecanoic acid was also employed (route B). Spectroscopic and elemental analyses enabled qualitative and quantitative characterization of products 4 and 6. In particular, solution-phase NMR spectroscopy realized convenient and informative analysis of the organically functionalized nanoparticle.[38,64,72,73]

In the IR spectra of **6-A** and **6-B**, prepared via routes A and B, respectively, the absorptions corresponding to N−H stretching, C−H stretching, C=O stretching, and N−H bending are observed at 3400, 2900, 1710, and 1650 cm$^{-1}$, respectively, indicating the formation of 6 (Figure 1). On the basis of the absorbance of C−H stretching at 2900 cm$^{-1}$, the relative intensity corresponding to N−H at 3400 and 1650 cm$^{-1}$ in **6-B** is larger than that in **6-A**, indicating that **6-B** is more functionalized with ω-aminododecanoate than **6-A**.

(70) Peng, X.; Komatsu, N.; Kimura, T.; Osuka, A. *J. Am. Chem. Soc.* **2007**, *129*, 15947−15953.

(71) Peng, X.; Komatsu, N.; Bhattacharya, S.; Shimawaki, T.; Aonuma, S.; Kimura, T.; Osuka, A. *Nature Nanotechnol.* **2007**, *2*, 361−365.

(72) Komatsu, N.; Kadota, N.; Kimura, T.; Osawa, E. *Chem. Lett.* **2007**, *36*, 398−399.

(73) Korokov, V. V.; Kulakova, I. I.; Tarasevich, B. N.; Lisichkin, G. V. *Diamond Relat. Mater.* **2007**, *16*, 2129−2132.

(74) Ando, T.; Ishii, M.; Kamo, M.; Sato, Y. *J. Chem. Soc. Faraday Trans.* **1993**, *89*, 1783−1789.

(75) Ando, T.; Yamamoto, K.; Suehara, S.; Kamo, M.; Sato, Y.; Shimosaki, S.; Nishitani-Gamo, M. *J. Chin. Chem. Soc.* **1995**, *42*, 285−292.

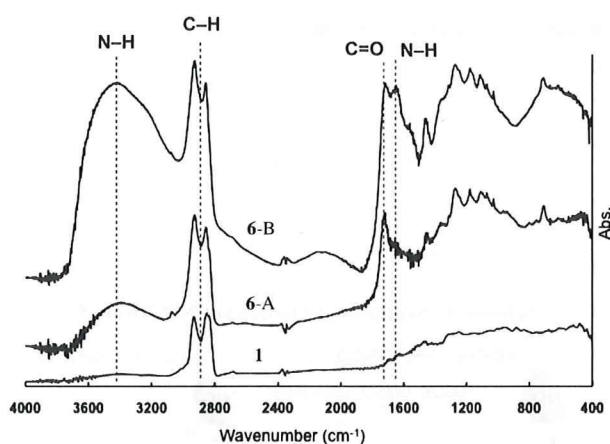(76) Huang, L.-C. L.; Chang, H.-C. *Langmuir* **2004**, *20*, 5879−5884.

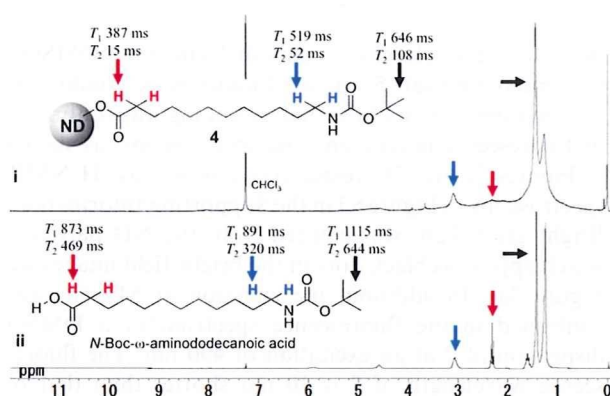**Figure 1.** Infrared (IR) spectra of **1**, **6-A**, and **6-B**.



**Figure 2.** Solution-phase $^1$H NMR spectra of (i) **4** and (ii) *N*-Boc-*ω*-aminododecanoic acid in CDCl$_3$. The relaxation times ($T_1$ and $T_2$) of *t*-Bu at 1.4 ppm (black arrow) and CH$_2$ at 2.3 ppm (red arrow) and CH$_2$ at 3.0 ppm (blue arrow) are indicated at the structures of **4** and *N*-Boc-*ω*-aminododecanoic acid.

Despite the estimated size being > 30 nm, **4** was well-dispersed in chloroform. Therefore, solution-phase $^1$H NMR spectroscopy was measured in CDCl$_3$ at room temperature (see Figure 2) and found to give slightly broad, but sufficiently resolved signals for the characterization of **4**. In comparison with the $^1$H NMR spectrum of *N*-Boc-*ω*-aminododecanoic acid (Figure 2ii), the corresponding resonances were observed at almost the same chemical shifts in the spectrum of Figure 2i, although they were broadened, probably because of shorter relaxation time and/or magnetic field inhomogeneity caused by differences in magnetic susceptibility between the solid particle and the liquid medium. In fact, the degree of broadening in the resonances correlates qualitatively to that of shortening in relaxation time, as shown in Figure 2. The same chemical shifts of the resonances on the spectra of Figures 2i and 2ii, mentioned above, indicate no anionic characteristics at the carboxylic function (namely carboxylate) and, therefore, no electrostatic interaction between the carboxylate and the hydrogenated ND surface. This is because the carboxylate makes the resonance of the adjacent hydrogens—highlighted by red arrows in the figures—shift upfield, which was confirmed by titration of triethylamine to *N*-Boc-*ω*-aminododecanoic acid in CDCl$_3$.

Covalent bonding between ND and the *N*-Boc-*ω*-aminododecanoate moiety was confirmed by the differences in the relaxation times ($T_1$ and $T_2$) between the hydrogens at the following three positions, as shown in Figure 2: (CH$_3$)$_3$C— (black arrow), —CH$_2$—NHCO— (blue arrow), and OCO—CH$_2$— (red arrow). All the $T_1$ and $T_2$ values (spin—lattice and spin—spin relaxation times, respectively) at the above positions in **4** are smaller than those in the *N*-Boc-*ω*-aminododecanoic acid. In addition, they become smaller (646 ms → 519 ms → 387 ms in $T_1$ and 108 ms → 52 ms → 15 ms in $T_2$), as the position of the hydrogens become closer to the ester group in the following order: (CH$_3$)$_3$C—, —CH$_2$—NHCO—, OCO—CH$_2$—. On the other hand, *N*-Boc-*ω*-aminododecanoic acid shows similar $T_1$ and $T_2$ values in these three types of hydrogens. The relaxation time studies suggest that (i) the mobility of *N*-Boc-*ω*-aminododecanoic acid was largely restricted after the reaction with ND and (ii) the mobility around the *C*-terminus (—CH$_2$CO$_2$—) is less than that around the *N*-terminus (—CH$_2$NHCO$_2$t-Bu). Therefore, we conclude that *N*-Boc-*ω*-aminododecanoic acid was firmly immobilized onto the ND surface through ester linkage. A remarkable site-specific reduction in $T_2$ (469 ms →15 ms) at OCO—CH$_2$— may provide another support for the ester linkage onto the ND surface; that is, ND intrinsically includes spins (unpaired electrons)[77,78] and the electron spins near ND surface are considered to significantly accelerate the relaxation ($T_2$) of nuclear spins of hydrogens close to the ND surface through spin—spin interaction. In the solution-phase $^{13}$C NMR of **4** (shown in Figure S2 in the Supporting Information), a broad resonance that originated from the diamond carbons was observed at 34 ppm,[72] along with a resonance assigned to (CH$_3$)$_3$C— at 28 ppm. These observations on the NMR spectra lead to the conclusion that the aminododecanoate moiety connects covalently to the ND surface through ester linkage.

To our knowledge, this is one of the largest nanoparticles giving clear NMR spectra in the solution phase, while a smaller size of ND (~5 nm) was reported to provide NMR spectra in solution phase.[38,64,67,72,73] Although solid-phase NMR spectroscopy has been frequently used for characterization of carbon materials, it is not so convenient for taking spectra with sufficient sensitivity and resolution, especially in the case of characterization of the organic moiety bound to a particle. In addition, the spectra obtained are not as informative as solution-phase NMR. Herein, it is disclosed that solution-phase NMR can be applied to characterize the surface chemical structures of relatively large nanoparticles.

Although IR spectra in Figure 1 derived a qualitative conclusion of route B as a more efficient route in the synthesis of **6**, the coverage of an ND surface with *ω*-aminododecanoate was evaluated quantitatively with elemental analysis (Table 1). The introduction of aminododecanoate increases the H, N, and O contents and

(77) Loubser, J.; Wyk, J. *Rep. Prog. Phys.* **1978**, *41*, 1201–1248.
(78) Dubois, M.; Guérin, K.; Petit, E.; Batisse, N.; Hamwi, A.; Komatsu, N.; Giraudet, J.; Pirotte, P.; Masin, F. *J. Phys. Chem. C* **2009**, *113*, 10371–10378.

**Table 1. Elemental Analyses of 1, 6-A, and 6-B, and the Estimated Atom Numbers**

| | 1 | | 6-A | | 6-B | |
|---|---|---|---|---|---|---|
| element | composition (wt %) | number of atoms[a] | composition (wt %) | number of atoms[a] | composition (wt %) | number of atoms[a] |
| H | 0.77 | $2.3 \times 10^5$ | 1.22 | $3.8 \times 10^5$ | 1.35 | $4.2 \times 10^5$ |
| C | 98.5 | $2.5 \times 10^6$ | 97.2 | $2.5 \times 10^6$ | 96.4 | $2.5 \times 10^6$ |
| N | 0 | 0 | 0.28 | $6.2 \times 10^3$ | 0.37 | $8.1 \times 10^3$ |
| O | 0 | 0 | 1.40 | $2.7 \times 10^4$ | 1.86 | $3.6 \times 10^4$ |

[a] The number of atoms is estimated based on the number of C atoms ($2.5 \times 10^6$) of a spherical ND (30 nm in diameter).

decreases the C content, because aminododecanoate has the following molecular formula: $C_{12}H_{24}NO_2$ (C, 67.2%; H, 11.3%; N, 6.5%; and O, 14.9% (by weight)). In comparison with 6-A, the H and N contents in 6-B are larger, but the C content is less, indicating clearly that 6-B is covered more densely with aminododecanoate groups than 6-A. This is consistent with the result of IR spectra (Figure 1), as described above; route B gave better coverage than route A, despite the three-step process. The reaction was reported to occur between carboxylic acid and the radical formed by hydrogen abstraction from the surface of 1 by benzoyl radical (PhCOO·) generated from benzoyl peroxide (BPO).[44,45] Therefore, the protection of the amino group with Boc may suppress the formation of the twitter ion ($^-_2OC(CH_2)_{11}NH_3^+$), accelerating the reaction of the ND radical with the amino acid. In addition, the Boc group increases the solubility of the reactant in DMF, facilitating the radical reaction.

If the functionalized ND (30 nm in diameter) has a spherical shape, each particle is calculated to consist of $2.5 \times 10^5$ C atoms.[79] Based on the number of C atoms in the ND core and the result of elemental analysis, the numbers of H, N, and O atoms can be estimated as shown in Table 1. The number of N atoms corresponds to that of the aminododecanoate introduced to the ND, because each functional group includes only one N atom ($C_{12}H_{24}\underline{N}O_2$) and nitrogen is not detected in 1. The ratio of the numbers of N atoms in 6-A and 6-B ($8.1 \times 10^3/6.2 \times 10^3 = 1.3$) indicates that 6-B is functionalized with aminododecanoate 30% more than 6-A. The numbers of H atoms increased from that in 1 are $1.5 \times 10^5$ in 6-A and $1.9 \times 10^5$ in 6-B. These numbers are almost equal to those derived by multiplying the corresponding number of N atoms by 24, which corresponds to the number of H atoms in aminododecanoate ($C_{12}\underline{H_{24}}NO_2$). Approximately 30% more coverage with the functionality in 6-B is also confirmed by the ratio of these numbers ($1.9 \times 10^5/1.5 \times 10^5 = 1.3$). On the other hand, the actual numbers of O atoms in 6-A and 6-B are larger than those estimated from the number of N atoms. This is probably because the radical generated on the ND also reacted with the water originally included in commercial BPO and with the benzoic acid generated in situ through the abstraction of hydrogen by benzoyl radical, giving hydroxyl and benzoate groups, respectively.

**Synthesis and Characterization of Fluorescent ND.** Fluorescent ND 7 was synthesized via the reaction of 5 with fluorescein succinimidyl ester, as shown in Scheme 3.

(79) Shenderova, O. A.; Zhirnov, V. V.; Brenner, D. W. *Crit. Rev. Solid State Mater. Sci.* **2002**, *27*, 227–356.

**Scheme 3. Synthesis of Fluorescent ND 7 from 5**
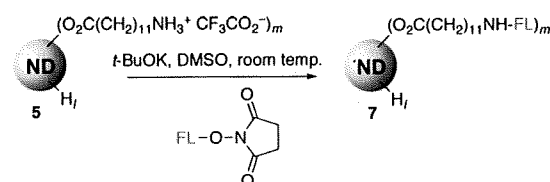


Because of the solubility in dimethyl sulfoxide (DMSO), the ammonium salt 5 was used under basic conditions. The immobilization of the fluorescent tag was confirmed by fluorescence microscopy and spectroscopy, as shown in Figures 3a and 3b, respectively, as well as $^1$H NMR spectroscopy in Figure S3 in the Supporting Information. Bright green light was emitted from the ND particles, which appear as black dots in the bright-field image (see Figure 3a). In addition, the emission at 540 nm was confirmed in the fluorescence spectrum of a DMSO dispersion of 7 at an excitation of 490 nm. The fluorescence wavelength of 7 is 10 nm shorter than that of succinimidyl ester of fluorescein under similar conditions in the fluorescence spectra shown in Figure 3b. This is probably due to the immobilization of the fluorescein onto the ND surface. In the $^1$H NMR spectrum of 7 dispersed in DMSO-$d_6$ (see Figure S3 in the Supporting Information), multiple signals were observed in the aromatic region (6.5−8.4 ppm), where no signals were detected before the immobilization of fluorescein. The resonance of $-CO_2H$ in fluorescein (see Scheme 1) was also observed as a broad signal at 10.2 ppm. On the IR spectrum of 7 (Figure S4 in the Supporting Information), absorption due to aromatic C−C bonds was appeared at $\sim 1600$ cm$^{-1}$, whereas no such peaks were observed on the spectrum of 6-B. These observations support the immobilization of fluorescein on the ND surface.

According to the molecular design mentioned above, the amino group apart from the ND surface formed an amide linkage with fluorescein, immobilizing the fluorescent tag covalently on the ND. Fluorescent ND was successfully obtained through the multistep organic transformations on the ND surface.

**Synthesis, Characterization, and Biological Application of Fluorescent ND Dispersible in a Buffer Solution.** For biomedical application of thus-synthesized ND, the fluorescent particle must be stably dispersed under a physiological environment. Therefore, a polyethylene glycol (PEG) moiety was designed to be introduced between the aminododecanoate and the fluorescent tag in 7 to add sufficient hydrophilicity for the ND to be

dispersed in PBS and cell culture medium. Surface functionalization to produce stable hydrosols is raised as a key aspect for biomedical application of ND in the very recent reviews.[61,63] To add hydrophilic functionality to the ND, we extend the concept of "functionalization partitioning" proposed by Dai from two dimensional (2D) to three dimensional (3D).[23] The functionalization partitioning of
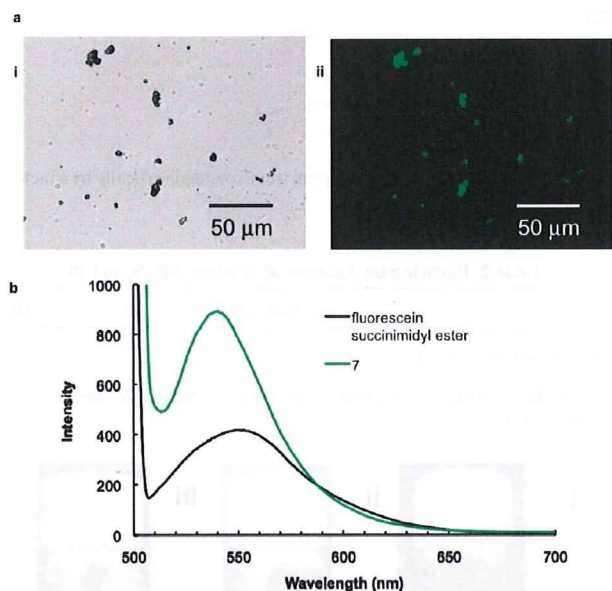


**Figure 3.** Characterization of fluorescent ND **7**: (a) bright-field image of **7** (panel i) and fluorescence image of **7** (panel ii) at an excitation of 470−490 nm and an emission of 515−550 nm, and (b) fluorescence spectra of **7** and fluorescein succinimidyl ester (Scheme 1) in DMSO at an excitation of 490 nm.
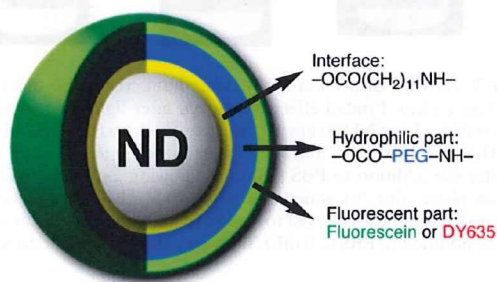


**Figure 4.** Schematic representation of the layered structure of fluorescent ND stably dispersed under a physiological environment.

carbon nanotubes was realized by imparting multiple functions at the different areas on the wide surface of carbon nanotubes.[23] On the other hand, the requisite functions are partitioned to the covalently connected layers above the ND surface in our case. A schematic representation of our 3D functionalization partitioning is shown in Figure 4. The functionalized ND designed here consists of four layers including the core, interfacial, hydrophilic, and luminescent segments from the center to the periphery. Since the surface area in one ND particle is not as large as that in a carbon nanotube, the 3D model is considered to be rational for the design of multifunctional ND.

The dispersible fluorescent ND was synthesized through multistep transformations of ND, shown in Scheme 4. The ammonium salt **5** was converted to **8** by reacting under basic conditions with $N$-Boc-$\omega$-amino acid derivative (molecular weight: ca. 5000) possessing PEG in the body and succinimidyl ester at the $C$-terminus. The introduction of PEG to **5** and the deprotection of Boc group in **8** were confirmed by solution-phase $^1$H NMR and $^{13}$C NMR, as shown in Figure 5 and Figure S5 (see the Supporting Information), respectively. With regard to the $^1$H NMR spectra of **8** and **9** shown in Figure 5, the hydrogens at PEG ($-OCH_2CH_2O-$) and dodecanoate ($-CH_2-$) were observed at 3.5 and 1.2 ppm, respectively, as singlets. However, the intensities of these resonances are largely different, because one PEG chain includes more than 100 ethylene oxide units ($-CH_2CH_2O-$), corresponding to more than 400 hydrogens, which are much more than the number of hydrogens in a dodecanoate moiety ($-CH_2-$). After the reaction of **8** in trifluoroacetic acid, the resonance corresponding to $t$-Bu at 1.35 ppm disappeared on the spectrum of **9**, which is indicative of deprotection of the Boc group in **8**. The downfield shift of the water signal from 3.3 ppm to 3.8 ppm supports the conversion of the Boc-protected amino group ($-NH$-Boc) to ammonium ($-NH_3^+$), because the proton from the ammonium is considered to cause the downfield shift of water in DMSO-$d_6$. In the $^{13}$C NMR spectra of **8** and **9** shown in Figure S5 (see the Supporting Information), the resonance of PEG was observed at 70 ppm. The signal of the ND core was observed at 34 ppm[72] only in the spectrum of **9**, probably because of its higher solubility in DMSO. The solution-phase NMR spectroscopies

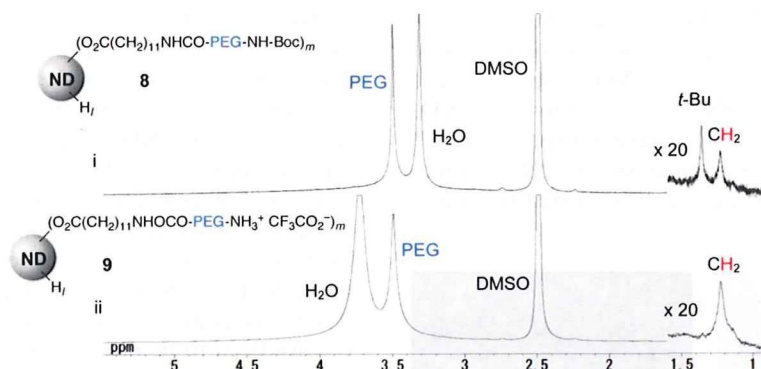**Scheme 4. Synthesis of Fluorescent ND 10 from 5.**
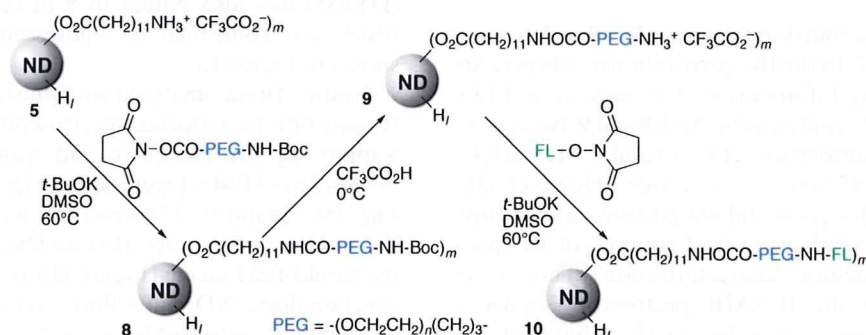
**Figure 5.** Solution-phase $^1$H NMR spectra of **8** (spectrum i) and **9** (spectrum ii) in DMSO-d$_6$. The range of 0.9−1.6 ppm was expanded vertically by a factor of 20 to clarify the relatively small resonances.
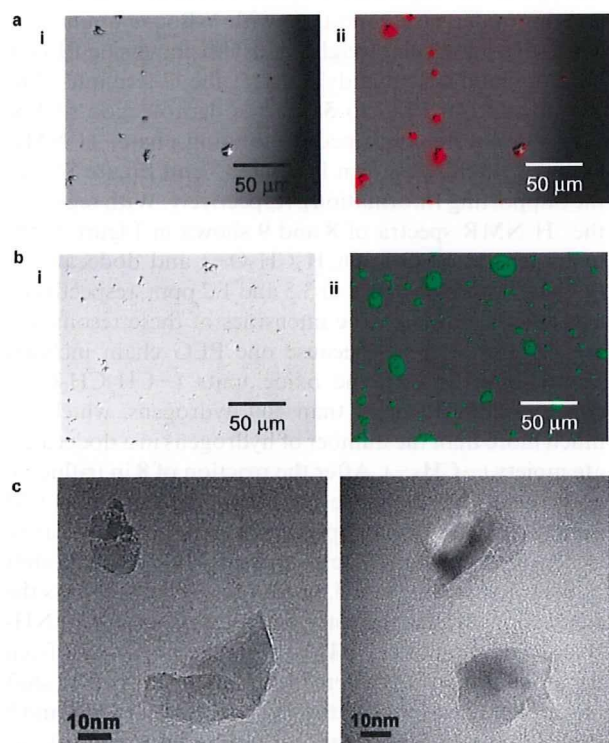


**Figure 6.** (a) Bright-field image (panel i) and fluorescence image (panel ii) of **10**, including DY635 as fluorescent tag instead of fluorescein, at an excitation of 630−650 nm and an emission of 671−693 nm, after merging with the bright-field image (panel i). (b) Bright-field image (panel i) and fluorescence image (panel ii) of **10**, at an excitation of 470−490 nm and an emission of 515−550 nm, after merging with the bright-field image (panel i). (c) TEM images of **10**.

**Table 2. Particle Size Analyses of Starting ND, 5, and 10**

|                      | starting ND$^a$ | 5$^b$ | 10$^b$ |
| -------------------- | --------------- | ----- | ------ |
| median diameter (nm) | 30              | 37    | 48     |

$^a$ ND provided by Tomei Diamond Co., Ltd. $^b$ Structures are depicted in Scheme 4.
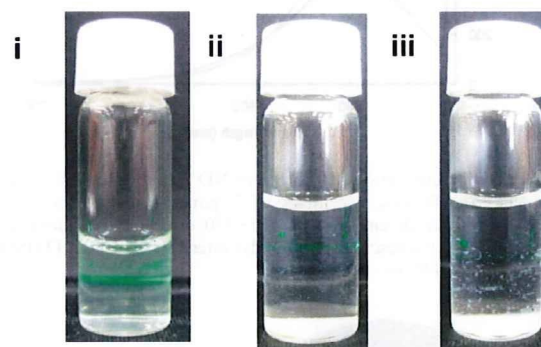


**Figure 7.** (i) PBS dispersion of **10** after more than one month, still exhibiting a clear Tyndall effect with green laser light. (ii) An aqueous solution (0.5 mL) of ND 30 nm in diameter, which was treated with mixed acid (H$_2$SO$_4$/HNO$_3$), was allowed to stand at room temperature for one day after the addition to PBS (2.0 mL), showing almost no ND in the solution phase. (iii) An aqueous solution (0.5 mL) of detonation ND (5 nm in diameter) was allowed to stand at room temperature for one day after the addition to PBS (2.0 mL), showing almost no ND in the solution phase.

support the organic transformations of **5** → **8** → **9** that are shown in Scheme 4. In the IR spectra shown in Figure S6 (see the Supporting Information), the existence of PEG was unambiguously confirmed in both **8** and **9**, because of the characteristic absorption of C−O and C−H stretching at 1100 and 2850 cm$^{-1}$, respectively. However, deprotection of the Boc group did not give any clear change on the IR spectrum, showing the limitation of IR spectroscopy for structural characterization. This is in marked contrast to the $^1$H NMR spectroscopy shown in Figure 5, where the signal due to the *t*-butyl group

disappeared after deprotection. In the final step, fluorescein was immobilized through amide linkage in a manner similar to that in the synthesis of **7** (see Scheme 3), providing **10**. The fluorescent tag emitting red light (DY635) was also bound to **9** in the same procedure, which was confirmed by fluorescence microscopy, as shown in Figure 6a.

Product **10** was analyzed with fluorescence microscopy (Figure 6b), fluorescence spectroscopy (Figure S7 in the Supporting Information), and transmission electron microscopy (TEM) (Figure 6c and Figure S8 in the Supporting Information). Fluorescence was observed in the fluorescence microscopy (Figure 6b(ii)) from the dots in the bright-field image (Figure 6b(i)), indicating that the functionalized ND emits fluorescence. Fluorescence at 518 nm was confirmed by an excitation at 490 nm in the
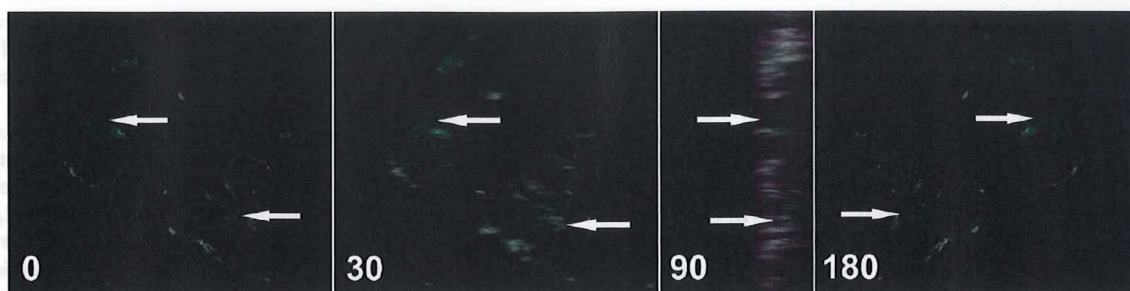
**Figure 8.** 3D images of HeLa cells at different angles after introduction of fluorescent ND **10**. The 3D image with a depth of 17 μm at 0° (left) was rotated by 360° around the vertical axis, as shown in the video presented in the Supporting Information. The images at 0°, 30°, 90°, and 180° are demonstrated here. The arrows in these images indicate the green fluorescence emitted from the NDs at the two positions.

fluorescence spectroscopy of **10** dispersed in PBS (shown in Figure S7 in the Supporting Information). TEM images (Figure 6c and Figure S8 in the Supporting Information) show that the particles have a variety of sizes (20–60 nm) and shapes. The median diameter of the particle was also confirmed by particle size analysis and was determined to be 48 nm (see Figure S9a in the Supporting Information). The median diameter of **10** is slightly larger than those of the starting ND (Figure S9b in the Supporting Information) and **5** (Figure S9c in the Supporting Information), as shown in Table 2, because of the coverage of ND with long chains including PEG groups. Although **7** is only dissolved in a few organic solvents (such as DMF and DMSO), **10** is stably dispersed not only in water, but also in PBS (see Figure 7i). Hydrophilicity of the PEG group remarkably increased the dispersibility of **10** and realized stable dispersion of the ND in PBS, although the dispersibility is not very high. The amount of ND dispersed in PBS was determined to be ~0.04 mg/mL. Since the dispersibility may be proportional to the number of PEG groups on the ND surface, it should increase by further optimization of the reaction conditions, enabling the immobilization of more PEG groups. On the other hand, NDs treated with a mixed acid (mixture of concentrated $H_2SO_4$ and $HNO_3$) at high temperature have been reported to have good dispersibility in water, but they are not dispersible in PBS, as shown in Figures 7ii and 7iii.[59,61,62,80]

Since **10** was also dispersed in the medium used for cell culture, we applied thus-synthesized ND to cell labeling. At the first attempt, HeLa cells were simply incubated in the presence of **10** in the culture medium. However, no introduction of **10** into the cells was observed upon fluorescence microscopy, probably because of the high dilution of **10**. Therefore, the complex of **10** with the hemagglutinating virus of Japan envelope (HVJ-E) was prepared and then applied to cell incubation. After 70 h, the cells were fixed on a chamber slide, washed with PBS, and observed using a confocal laser-scanning microscope. As shown in the 3D images of the cells (Figure 8) and the video presented in the Supporting Information, **10** was unambiguously introduced into the HeLa cells. The fluorescence originating from **10** was observed in the

perinuclear cytoplasmic vesicles, suggesting that **10** was incorporated into the endocytic vesicles.

For more biomedical applications of the ND, targeting specificity could be also incorporated in **10** by adding one more outer conjugate shell that possesses peptides such as RGD (Arg-Gly-Asp) and LFPLH (Leu-Phe-Pro-Leu-His) or replacing some of the fluorescent tag to the peptides in the outmost layer in **10**.[81,82]

## Conclusion

We have shown that multiple steps of organic transformation and characterization sequence constructed nanodiamond (ND) with multifunctions, including fluorescence and dispersibility under a physiological environment. First, ω-aminododecanoic acid was immobilized as the interface between the ND surface and the subsequent functionality, because direct introduction of bulky functionality is considered to be difficult. The ω-aminododecanoate of the ND was well-characterized by IR, solution-phase NMRs, and elemental analysis. The hydrophilic and fluorescent segments including PEG and fluorescein or DY635, respectively, were introduced successively through the amide linkages. These organic transformations on the ND surface enabled the assembly of fluorescent ND stably dispersed under a physiological environment. The fluorescent and hydrophilic functions are partitioned to the two outermost layers of the ND. The ND thus synthesized was introduced into HeLa cells, which was imaged fluorescently. In principle, more functions such as targeting specificity and more imaging modalities can be incorporated into ND by extending the outer layer (in other words, by expanding the concept of the 3D partitioning functionalization).

## Experimental Section

**Materials.** ND powder with a median diameter of 30 nm is prepared by size-separating the powdered diamond from the bulk synthesized by a static high-pressure high-temperature (HPHT) method; it was kindly provided by Tomei Diamond Co., Ltd.[83] Detonation ND (5 nm in diameter), used in Figure 7iii, is

(80) Neugart, F.; Zappe, A.; Jelezko, F.; Tietz, C.; Boudou, J. P.; Krueger, A.; Wrachtrup, J. *Nano Lett.* **2007**, *7*, 3588–3591.

(81) Liu, Z.; Tabakman, S.; Welsher, K.; Dai, H. *Nano Res.* **2009**, *2*, 85–120.

(82) Liu, Z.; Cai, W.; He, L.; Nakayama, N.; Chen, K.; Sun, X.; Chen, X.; Dai, H. *Nature Nanotechnol.* **2007**, *2*, 47–52.

(83) Morita, Y.; Takimoto, T.; Yamanaka, H.; Kumekawa, K.; Morino, S.; Aonuma, S.; Kimura, T.; Komatsu, N. *Small* **2008**, *4*, 2154–2157.

purchased from NanoCarbon Research Institute Co., Ltd.[84] Hydrogenated ND **1** and aminated ND **2** were prepared by Tomei Diamond Co., Ltd., according to the reported procedure.[74,75] Succinimidyl ester of fluorescein was purchased from Thermo Fisher Scientific, Inc. Boc-protected aminododecanoic acid was prepared from ω-aminododecanoic acid (Wako Pure Chemical Industries, Ltd.) and di-*t*-butyl dicarbonate (Wako Pure Chemical Industries, Ltd.). Commercial benzoyl peroxide (BPO), including 25% water (Nacalai Tesque, Inc.), was used for the radical reaction without purification. The ND **5** was PEGylated using commercial α-3-(*N*-*t*-butyloxycarbonylamino)propyl-ω-(succinimidyloxycarboxy), polyoxyethylene (SUNBRIGHT BO-050TS, NOF Co.). All other reagents and solvents were purchased from commercial sources and used without purification.

**Equipments.** IR spectral measurements were conducted using IR Prestige-21 (Shimadzu Co.). $^1$H (270 MHz) and $^{13}$C (67.5 MHz) NMR spectra were recorded on a JEOL Model JNM-EX270 spectrometers. The relaxation times were calculated using the EXcalibur program for Windows (version 4.1). Particle size analysis was performed on a Nanotrac UPA-UT151 system (Microtrac, Inc.). Fluorescence spectra were measured on an F-4500 (Hitachi, Ltd.). Fluorescence and bright-field images were obtained with a BX61 system (Olympus Co.). Three-dimensional images of the cells were obtained with a confocal laser-scanning microscope (C1si, Nikon Co.). Elemental analyses of CHN and O were performed at Integrated Center for Sciences, Ehime University and on a VarioMICRO-cube (Elementar Analysensysteme GmbH), respectively.

**Synthesis of 6-A from 1.** Aminododecanoic acid (381 mg, 1.77 mmol) and BPO (105 mg, 0.432 mmol) were added to a suspension of **1** (40.1 mg) in DMF (10 mL). After the suspension was sonicated at 75 °C for 2 h, a 1:1 mixture of ethyl acetate: hexane (60 mL) was added to the suspension. Filtration followed by washing with acetic acid, triethylamine, water, and methanol gave 41.1 mg of black solid, which was characterized by IR (see Figure 1).

**Synthesis of 4 from 1.** To a suspension of **1** (0.800 g) in DMF (200 mL) were added *N*-Boc-ω-aminododecanoic acid (11.2 g, 35.4 mmol) and BPO (2.06 g, 8.52 mmol). After the suspension was sonicated at 75 °C for 2 h, a 1:1 mixture of ethyl acetate: hexane (60 mL) was added to the suspension. The solid was recovered from the suspension by centrifugation at 18 500 *g* several times and was washed with ethyl acetate, triethylamine, water, and methanol, giving 0.823 g of black solid. The product was characterized by $^1$H NMR (see Figure 2) and $^{13}$C NMR (see Figure S2 in the Supporting Information).

**Deprotection of Boc from 4.** A suspension of **4** in trifluoroacetic acid (1.0 mL) was stirred at 0 °C for 5 min. After adding chloroform, the suspension was centrifuged at 18 500 *g*. The precipitates were washed with chloroform several times and dried in vacuo, giving black solid **5** (16.2 mg). After washing with triethylamine, the amine **6-B** was characterized by IR (see Figure 1).

**Synthesis of Fluorescent ND 7 from 5.** Succinimidyl ester of fluorescein (2.02 mg, 4.27 μmol) and potassium *t*-butoxide (1.04 mg, 9.27 μmol) were added to a suspension of **5** (10.0 mg) in dry DMSO (0.15 mL). After stirring at room temperature for 2 h under argon atmosphere, the reaction was quenched by the addition of diethyl ether (10 mL) and the reaction mixture was filtered. The recovered solid was washed with triethylamine/methanol, methanol, and water, and dried in vacuo to give black solid **7** (9.55 mg).

The fluorescent ND was characterized by fluorescence microscopy (see Figure 3a) and spectroscopy (see Figure 3b), $^1$H NMR (see Figure S3 in the Supporting Information) and IR (see Figure S4 in the Supporting Information).

**Synthesis of Fluorescent ND 10 from 5.** To a suspension of **5** (0.100 g) in dry DMSO (1.50 mL) were added α-3-(*N*-*t*-butyloxy-carbonylamino)propyl-ω-(succinimidyloxycarboxy)polyoxyethylene (0.300 g, 63.1 μmol) and potassium *t*-butoxide (10.0 mg, 89.2 μmol). The resulting suspension was stirred at 60 °C for 18 h under argon atmosphere. After adding diethyl ether (10 mL), the suspension was filtered, and the solid was washed with triethylamine/methanol, methanol, and water. Black solid **8** (96.8 mg) was obtained after drying in vacuo.

Deprotection of the Boc group was accomplished by adding **8** (50.0 mg) in trifluoroacetic acid (1.0 mL). After stirring at 0 °C for 5 min, the reaction was quenched by the addition of chloroform (15 mL), and the resulting suspension was centrifuged at 18 500 *g*. The recovered solid was washed with chloroform and dried in vacuo to give black solid **9** (38.4 mg). $^1$H NMR and $^{13}$C NMR studies, as well as IR spectroscopy of **8** and **9** are shown in Figures 5, S5 (in the Supporting Information), and S6 (in the Supporting Information), respectively.

Succinimidyl ester of fluorescein (5.02 mg, 3.17 μmol) and potassium *t*-butoxide (0.80 mg, 7.13 mmol) were added to a suspension of **9** (5.02 mg) in dry DMSO (0.12 mL). After stirring at 60 °C for 18 h under an argon atmosphere, the reaction was quenched by the addition of diethyl ether (6.0 mL), and the reaction mixture was filtered. The recovered solid was washed with triethyl amine/methanol, methanol, and water, and then it was dried in vacuo to give black solid **10** (4.06 mg). Fluorescence from ND was confirmed by fluorescence microscopy (see Figure 6b) and spectroscopy (see Figure S7 in the Supporting Information).

**Introduction of Fluorescent ND 10 into Cultured HeLa Cells.** HeLa cells ($5 \times 10^4$ cells per well in 4-well LabTek chamber slides [BD bioscience]) cultured in Dulbecco's modified Eagle's medium (DMEM) containing 10% fetal bovine serum were incubated for 70 h with the complex between the hemagglutinating virus of Japan envelope (HVJ-E) and fluorescent ND **10**. The complex was prepared using HVJ-E transfection kit (GenomONE, Ishihara Sangyo Kaisha, Ltd.) according to the supplier's recommendations and was applied to cell incubation at a concentration of ~1 μg/mL of **10**. The cells were fixed with 1% buffered formaldehyde and 70% ethanol, washed with PBS, and mounted with glycerol. Both optical and fluorescent images of the cells were obtained under identical conditions using a confocal laser-scanning microscope and overlapped to prepare the 3D images (see Figure 8) and the video provided in the Supporting Information. The 3D image was composed of 27 scan images to a depth of 17 μm.

(84) Krüger, A.; Kataoka, F.; Ozawa, M.; Fujino, T.; Suzuki, Y.; Aleksenskii, A. E.; Vul', A. Y.; Osawa, E. *Carbon* **2005**, *43*, 1722–1730.

*Article*

*Chem. Mater., Vol. 22, No. 11, 2010* 3471

**Supporting Information Available:** Bright-field and fluorescent images of **3**, and infrared spectra of **2** and **3** (Figure S1). Solution-phase $^{13}$C NMR of **4** and *N*-Boc-$\omega$-aminododecanoic acid in CDCl$_3$ (Figure S2) and solution-phase $^1$H NMR spectra of **7** in DMSO-d$_6$ (Figure S3). Infrared spectra of **6-B** and **7** (Figure S4). Solution-phase $^{13}$C NMR of **8** and **9** in DMSO-d$_6$ (Figure S5). Infrared spectra of **6-B, 8**, and **9** (Figure S6). Fluorescence spectrum of **10** dispersed in PBS (Figure S7). TEM photomicrographs of **10** (Figure S8). Particle size analyses of **10** dispersed in PBS, the starting ND dispersed in water, and **5** dispersed in DMSO (Figure S9). (PDF) Video showing rotating 3D imaging of HaLa cells, in which **10** was introduced. This material is available free of charge via the Internet at http://pubs.acs.org.

# Simple PEG Conjugation of SPIO via an Au–S Bond Improves Its Tumor Targeting Potency as a Novel MR Tumor Imaging Agent

Hiroki Kojima,[†] Yohei Mukai,[*,†] Mai Yoshikawa,[†] Kazumasa Kamei,[†] Tomoaki Yoshikawa,[†] Masahito Morita,[‡,§]
Toshiro Inubushi,[§] Takao A Yamamoto,[‖] Yasuo Yoshioka,[†,⊥] Naoki Okada,[†] Satoshi Seino,[‖] and
Shinsaku Nakagawa[*,†,⊥]

Graduate School of Pharmaceutical Sciences and Center for Advanced Medical Engineering and Informatics, Osaka University,
1–6 Yamadaoka, Suita, Osaka 565–0871, Japan, Immunology Frontier Research Center, Osaka University,
1-3 Yamadaoka, Suita, Osaka 565–0871, Japan, Graduate School of Engineering, Osaka University, 2–1 Yamadaoka,
Suita, Osaka 565–0871, Japan, and Biomedical MR Science Center, Shiga University of Medical Science, Tsukiwa-cho, Seta,
Otsu, Shiga, 520-2192, Japan. Received November 10, 2009; Revised Manuscript Received April 11, 2010

Gold/iron oxide magnetic nanoparticles are hybrid nanoparticles containing a core of magnetic iron oxide and surface colloidal gold, which allows for various biomaterials to be immobilized on the surface of the iron oxide nanoparticles *via* colloidal gold. Here, we developed a novel magnetic resonance (MR) imaging agent to broaden the MR tumor-imaging spectrum of superparamagnetic iron oxide nanoparticles (SPIO), e.g., Feridex, a clinical MR imaging agent for diagnosing liver cancer. Au/Feridex was synthesized by electron beam irradiation, and thiol-modified poly(ethylene glycol) (PEG-SH) was easily conjugated to its surface via an Au–S bond without the need for any chemical reactions. PEG conjugation of Au/Feridex enhanced its accumulation in Meth-A tumor tissue and decreased its accumulation in normal liver tissue. In addition, MRI using PEG-Au/Feridex, in contrast to MRI using unmodified Au/Feridex and Feridex, detected B16BL6 and Meth-A tumor tissues *in vivo*. This finding indicates that PEG-Au/Feridex is useful for diagnosing various types of tumors. In addition, because the synthesis of PEG-Au/Feridex is simple and high yields are easily produced, PEG-modified SPIO for tumor diagnosis can be prepared on an industrial scale with low cost.

## INTRODUCTION

Superparamagnetic iron oxide (SPIO) is a potent contrast agent for magnetic resonance imaging (MRI) (1–4), represented by Feridex (AMAG Pharmaceuticals, Inc., MA) and Resovist (Bayer Schering Pharma AG., Germany). These compounds contain a core iron oxide nanoparticle coated with a dextran polymer. SPIO decreases the signal intensity on $T_2$ ($T_2^*$)-weighted MR images and is clinically used for diagnosing liver cancer (5–7). SPIO is expected to improve the accuracy and specificity of cancer diagnoses in combination with other diagnostic tools such as computed tomography and ultrasonography (8).

SPIO in the blood is rapidly taken up by the reticular endothelial system (RES) like the hepatic specialized macrophages and Kuppfer cells, resulting in a high accumulation in healthy liver tissue (9, 10). On the other hand, SPIO does not accumulate in liver tumor tissue lacking Kuppfer cells and does not decrease the signal intensity of tumors, which leads to an increased contrast between healthy liver tissue and tumor tissue (8–10). Because this mechanism inhibits the distribution of SPIO to other tissues, however, the application of SPIO is limited to the diagnosis of liver cancer. Therefore, many researchers have attempted to develop novel contrast agents for various types of tumors by improving the SPIO (1, 11, 12).

Surface modification of SPIO with various biomaterials to inhibit RES uptake is considered effective for targeting tumors (1). In particular, conjugation with a water-soluble polymer on the SPIO surface is an effective method of inhibiting RES uptake, subsequently prolonging the half-life of SPIO in the blood. A longer blood half-life of SPIO allows for specific accumulation in tumor tissue by an enhanced permeability and retention effect (EPR effect) (1, 13–18). Many methods of surface modification have been reported: encapsulation of SPIO into nanoimmunoliposomes (13), conjugation of SPIO with polymers such as poly(ethylene glycol) (PEG), poly(ethylene oxide), and dextran (17, 19). These approaches, however, require specially designed polymer molecules or complicated preparation methods (20, 21). There is therefore strong interest in developing a simple and easy method of conjugating functional molecules to the SPIO surface.

We developed gold/iron magnetic nanoparticles that are easily synthesized by electron beam irradiation of a mixture of iron oxide nanoparticles and Au solution (22). Using this method, gold/iron magnetic nanoparticles are obtained in extremely high yield (almost 100%). Colloidal gold forms a strong Au–S bond with a thiol group just by mixing, without any catalysts or linker molecules (22–25). This property is useful for conjugating various polymers or biomolecules on the nanoparticle surface. As one application, we previously reported that an adenovirus vector (Ad) could be easily immobilized on the gold/iron nanoparticle via the Au–S bond, allowing the Ad/nanoparticle

* Corresponding authors. Yohei Mukai, Ph.D., Department of Biotechnology and Therapeutics, Graduate School of Pharmaceutical Sciences, Osaka University, 1–6 Yamadaoka, Suita, Osaka 565–0871, Japan. Tel: +81-6-6879-8178, Fax: +81-6-6879-8179, E-mail: yohe@phs.osaka-u.ac.jp. Shinsaku Nakagawa, Ph.D., Department of Biotechnology and Therapeutics, Graduate School of Pharmaceutical Sciences, Osaka University, 1–6 Yamadaoka, Suita, Osaka 565–0871, Japan. Tel: +81-6-6879-8175, Fax: +81-6-6879-8179, E-mail: nakagawa@phs.osaka-u.ac.jp.
    † Graduate School of Pharmaceutical Sciences, Osaka University.
    ‡ Immunology Frontier Research Center, Osaka University.
    § Shiga University of Medical Science.
    ‖ Graduate School of Engineering, Osaka University.
    ⊥ Center for Advanced Medical Engineering and Informatics, Osaka University.

complex to be introduced into cells by magnetic force, resulting in great improvement in the gene transduction efficacy of the Ad (*23*). In the present study, we synthesized a gold/iron magnetic nanoparticle using Feridex, a clinically available SPIO for liver cancer diagnosis, as its core (Au/Feridex). We coated the surface of Au/Feridex using a thiol-modified PEG to inhibit its accumulation in the liver, thereby extending its half-life in the blood, and to target tumors by the EPR effect. We evaluated the efficacy of PEG-conjugated Au/Feridex (PEG-Au/Feridex) as a tumor contrast agent in tumor-bearing mice.

## EXPERIMENTAL PROCEDURES

**Au/Feridex Synthesis.** Feridex (Advanced Magnetics, Inc.) was dispersed at a concentration of 0.1 g/L in an aqueous solution containing 0.5 mM AuHCl$_4$, 4.125 mM 2-propanol, and 10 g/L poly(vinyl alcohol) (PVA). The dispersion was poured into a glass vial and irradiated with an electron beam at a dose of 6 kGy. Au/Feridex was purified by high-speed centrifugation and redispersed in distilled water. The size was measured using a dynamic light scattering method with a Z-sizer 3000-HS (Malvern Instruments Ltd., UK).

**Cell Line.** Mouse melanoma cells (B16BL6) were kindly provided from Kobegakuin University. B16BL6 cells were cultured in Minimum Essential Medium (Sigma-Aldrich, St. Louis, MO) containing 7.5% fetal bovine serum (Invitrogen Corporation, Carlsbad, CA) and Antibiotic-Antimycotic Mixed Solution (Nacalai Tesque Inc., Japan). RAW264.7 cells were purchased from American Type Culture Collection. RAW264.7 cells were cultured in Dulbecco's Modified Eagle's Medium (Wako Pure Chemical Industries Ltd., Osaka, Japan) containing 10% fetal bovine serum and Antibiotic-Antimycotic Mixed Solution. Meth-A cells were kindly provided by the Institute of Development, Aging, and Cancer of Tohoku University. Meth-A cells were maintained by intraperitoneal passage in BALB/c mice.

**Transmission Electron Microscopy (TEM) Observation of Feridex and Au/Feridex.** The morphologies of the Feridex and Au/Feridex were observed by a TEM (H-8100T, Hitachi Ltd., Tokyo, Japan) operated at 200 kV. The typical image from several TEM micrographs is shown in this report.

**Preparation of PEG-Conjugated Au/Feridex (PEG-Au/Feridex).** Au/Feridex and thiol-modified PEG (PEG-SH, MW = 5000 Da; NOF Corporation, Japan) were mixed at a ratio of 1:1 (1 μmol PEG-SH/mg Fe) in Au/Feridex. The mixture was incubated at room temperature for 1 h and then purified by high-speed centrifugation (28 000 rpm, 30 min). The concentrations of Fe and Au were determined using an inductively coupled plasma (ICP) spectrometer ICPS-7500 (Shimadzu Corporation, Japan).

**PVA Test—Cross-Linking of PEGylated Contrast Agents.** Contrast agents (Feridex or Au/Feridex) and PEGs (PEG-SH or nonmodified PEG, MW = 5000 Da; Wako Pure Chemical Industries Ltd.) were mixed at a ratio of 1:1 (1 μmol PEGs/mg Fe). After 1 h incubation at room temperature, the mixtures were purified by high-speed centrifugation (100 000 × *g*, 30 min), and the pellet was resuspended with distilled water. An aliquot of 5 mg Fe/mL of these reactants was mixed with an equal volume of 30% PVA (Wako Pure Chemical Industries Ltd.) and incubated at room temperature for 1 h. Cross-linking between PVA and PEG resulted in a precipitate that contained the nanoparticles (*26*).

**Quantification of PEG-SH Immobilized on Contrast Agents.** Feridex and Au/Feridex were mixed with PEG-SH at a ratio of 1:1 (1 μmol PEGs/mg Fe). After 1 h incubation at room temperature, the mixtures were purified by high-speed centrifugation (100 000 × *g*, 30 min). The amount of sulfur

contained in PEG-SH in each sample was then determined using an ICP spectrometer.

***In Vitro* MRI.** Feridex, Au/Feridex, and PEG-Au/Feridex were diluted with distilled water to contain the same iron concentration (50 μg/mL, 10 μg/mL, and 2 μg/mL). T$_2$-weighted images (multislice spin-echo coronal images; TR = 2000 ms, TE = 69 ms) of these solutions were obtained with a 1.5 T MRI (MRminiSA; DS Pharma Biomedical Co., Ltd., Japan).

***In Vivo* Blood Clearance.** BALB/c mice were intravenously injected with 1 mg Fe in contrast agents (Feridex, Au/Feridex, and PEG-Au/Feridex). Blood samples were collected at 2, 5, 10, 30, and 60 min postinjection. T$_2$-weighted images of these samples were obtained with a 1.5 T MRI (MRminiSA; DS Pharma Biomedical Co., Ltd., Japan). The signal intensity of each sample on the MR image was analyzed using *Image J* software (National Institutes of Health, USA). The iron concentration of the samples was calculated based on the correlation between the signal intensity and the iron concentration of Feridex. All studies involving animals were approved by the institute's animal care and use committee.

***In Vivo* Distribution.** Meth-A cells (5 × 10$^5$ cells/100 μL) were injected intradermally into the abdomen of 6-week-old BALB/c mice. When the tumor size reached 10 mm in diameter, 1 mg Fe/200 μL of each contrast agent (Au/Feridex, PEG-Au/Feridex) was injected intravenously into the mice (*n* = 3 mice per group). The mice were killed, and the tumor and liver were extracted at 1 or 24 h postinjection and immediately freeze-dried. Radiation was counted after irradiation of vials containing samples in a nuclear reactor (JRR-3 in Japan Atomic Energy Agency, Ibaragi, Japan) with a thermal neutron flux of 5.2 × 10$^{17}$ neutrons/cm/s for 20 min. After a delay of 4 to 5 days, irradiated samples were counted by computer-based γ-ray spectrometry on a Ge detector for 2000 s, and then the peak area of 412 keV γ-rays from $^{198}$Au elements was measured using a multichannel pulse height analyzer with automatic dead time (<10%) correction.

***In Vivo* MR Tumor Imaging.** C57BL/6 mice (6 weeks old) were injected intradermally in the abdomen with 5 × 10$^5$ cells/100 μL of B16BL6 cells. Meth-A tumor-bearing mice were prepared as described below. When the tumors were 10 mm in diameter, 1 mg Fe/200 μL of each contrast agent (Feridex, Au/Feridex, PEG-Au/Feridex) was injected into the mice (*n* = 3 mice per group). MRI studies were performed with MRminiSA (DS Pharma Biomedical Co., Ltd.). Tumor-bearing mice were anesthetized with a 1.5% isoflurane/air mixture and maintained at 37 °C inside the magnet. All images were obtained as T$_2$-weighted images (multislice spin-echo axial images; TR = 2000 ms, TE = 69 ms). MRI scans were performed before and 1 h after the injection.

**Iron Staining of Tumor Sections.** After *in vivo* MRI analysis, the tumor and liver were extracted and fixed with 4% paraformaldehyde followed by sequential immersion in 10%, 20%, and 30% sucrose solutions. Tissues were frozen in OCT compound (Sakura Finetek Inc., Torrance, CA) with liquid nitrogen and sectioned at 10 μm using a cryostat (CM1850; Leica Microsystems GmbH). Sections were stained with Prussian blue to detect the particles of Feridex, Au/Feridex, and PEG-Au/Feridex. Sections were stained with 1% potassium hexacyanoferrate (II)-trihydrate in 0.1 M HCl followed by counterstaining with 0.5% eosin Y ethanol solution.

## RESULTS

**Synthesis of PEG-Au/Feridex.** Au/Feridex was synthesized by electron beam irradiation of the mixture of AuHCl$_4$ and the Feridex solution. Synthesis of Au/Feridex was confirmed by transmission electron microscopy (Figure 1). Au/Feridex was visualized as colloidal gold nanoparticles (black particles) on
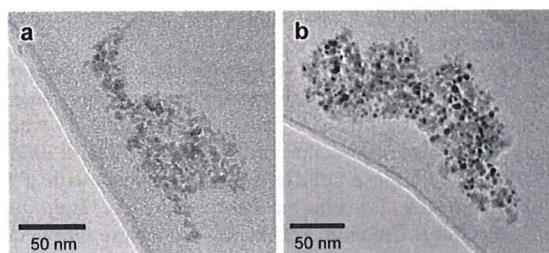
**Figure 1.** Transmission electron microscopy image of (a) Feridexand (b) Au/Feridex.

the surface of Feridex (gray particles; Figure 1b). Unreacted Feridex, i.e., without colloidal gold, was not observed in this solution. The ratio of Au/Fe was determined as 0.944 Au/Fe by weight using an ICP spectrometer.

PEG conjugation of Au/Feridex was performed by mixing PEG-SH (MW = 5000 Da) with Au/Feridex. PEG conjugation was confirmed by a PVA test, in which PEG-modified particles form a precipitate due to hydrogen bonding between PEG and PVA (26). Precipitation was observed only in the PEG-SH and Au/Feridex mixture, and there was no precipitate in the other mixtures (PEG-SH and Feridex, PEG and Au/Feridex, Au/Feridex alone; Figure 2). This findings indicated that PEG modification of Feridex was achieved by an Au−S bond.

**Characterization of PEG-Au/Feridex.** We measured the amount of PEG-SH immobilized on Au/Feridex using an ICP spectrometer. The amount of immobilized PEG-SH on Au/Feridex was 1.58 mg PEG-SH/mg Fe (1.74 mg PEG-SH/mg Au) and the amount immobilized on Feridex was 0.038 mg. This finding also suggests that PEG-SH was efficiently immobilized on Au/Feridex via Au−S bonds.

We measured the hydrodynamic size of these contrast agents (Feridex, Au/Feridex, and PEG-Au/Feridex) using a dynamic light scattering method. The hydrodynamic size of Feridex, Au/Feridex, and PEG-Au/Feridex was 69.4 nm, 163.9 nm, and 153.6 nm, respectively. Notably, the size of PEG-Au/Feridex (153.6 nm) was smaller than that of Au/Feridex (163.9 nm), suggesting that the state of dispersion was improved by PEG conjugation. The state of dispersion is an important factor in tumor targeting using the EPR effect (27, 28). Therefore, this result suggests that PEG-Au/Feridex may be able to effectively target tumors. PEG-Au/Feridex was not cytotoxic to RAW264.7 cells at a concentration of 300 $\mu$g Fe/mL (Supporting Information Figure S1). In fetal bovine serum at 37 °C, the Au−S bond remained unbroken after 1 h incubation (Supporting Information Figure S2). Moreover, PEG-Au/Feridex did not aggregate under this condition (data not shown). These results suggested that this
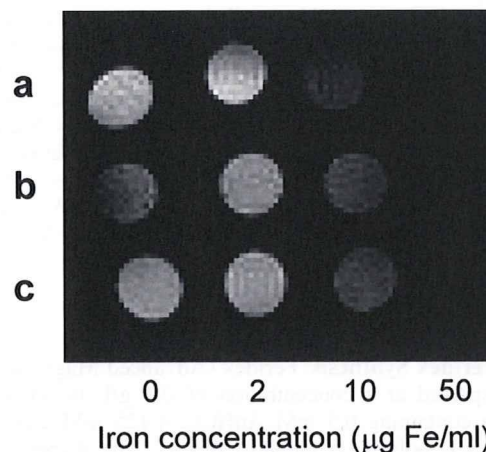


**Figure 3.** $T_2$-weighted images of each contrast agent. (a) Feridex, (b) Au/Feridex, and (c) PEG-Au/Feridex were diluted to the same iron concentration with distilled water. $T_2$-weighted images (spin-echo sequence: TR = 2000 ms, TE = 69 ms) were obtained using MRminiSA.

conjugation method using the Au−S bond is suitable for *in vivo* applications.

We then evaluated the transverse $T_2$ relaxation time of the three contrast agents using *in vitro* MRI images. All the contrast agents showed relaxation at an iron concentration of 10 $\mu$g/mL (Figure 3). These results indicate that the $T_2$ relaxation time was maintained after modification of colloidal gold and PEG-SH, suggesting that PEG-Au/Feridex and Feridex, a clinically used contrast agent, have a nearly equal $T_2$ relaxation.

**Distribution of Each Contrast Agent.** The efficacy of PEG modification was estimated by analyzing the blood clearance of Feridex, Au/Feridex, and PEG-Au/Freidex. Blood concentrations of each contrast agent were measured after intravenous injection into mice. The initial Fe concentration in the blood of mice injected with PEG-Au/Feridex was higher than in mice injected with Feridex and Au/Feridex (Figure 4). In addition, the clearance of PEG-Au/Feridex was moderate compared with that of Feridex and Au/Feridex (Figure 4). These findings suggest that the blood concentration of the imaging agent is increased by PEG modification.

We then evaluated the accumulation of the contrast agent in the liver and tumor. Au/Feridex and PEG-Au/Feridex were intravenously injected into Meth-A tumor-bearing BALB/c mice. At 1 h postinjection, the distribution in the liver and tumor tissues was determined by radiochemical neutron
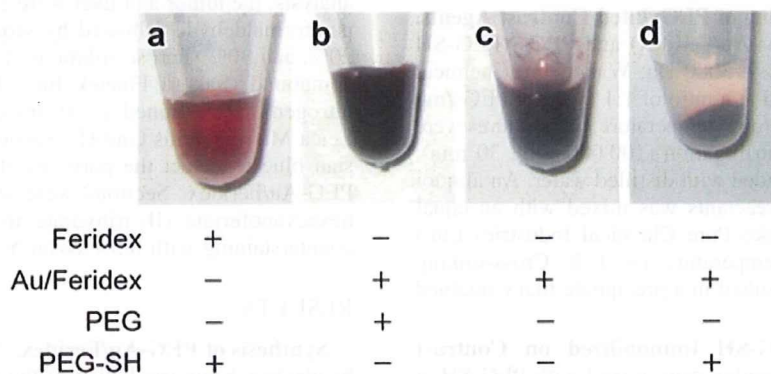


| | a | b | c | d |
|---|---|---|---|---|
| Feridex | + | − | − | − |
| Au/Feridex | − | + | + | + |
| PEG | − | + | − | − |
| PEG-SH | + | − | − | + |

**Figure 2.** Confirmation of PEG-conjugation to Au/Feridex. PEGs (nonmodified PEG and thiol-modified PEG) were mixed with 5 mg Fe/mL of contrast agents (Feridex and Au/Feridex), as shown in the figure, and purified by high-speed centrifugation. The purified mixtures were mixed with PVA to a final concentration of 15% PVA and incubated overnight at room temperature.